Journal of Applied Physics

Hyperbolic metamaterials: From dispersion manipulation to applications

Cite as: J. Appl. Phys. **127**, 071101 (2020); https://doi.org/10.1063/1.5128679
Submitted: 20 September 2019 . Accepted: 21 January 2020 . Published Online: 18 February 2020

Zhiwei Guo, Haitao Jiang, and Hong Chen

Journal of Applied Physics TUTORIAL scitation.org/journal/jap

Hyperbolic metamaterials: From dispersion manipulation to applications

Cite as: J. Appl. Phys. **127**, 071101 (2020); doi: 10.1063/1.5128679
Submitted: 20 September 2019 · Accepted: 21 January 2020 ·
Published Online: 18 February 2020

Zhiwei Guo, Haitao Jiang,[a] and Hong Chen[a]

AFFILIATIONS

Key Laboratory of Advanced Micro-structure Materials, MOE, School of Physics Science and Engineering, Tongji University, Shanghai 200092, China

[a]**Authors to whom correspondence should be addressed:** jiang-haitao@tongji.edu.cn and hongchen@tongji.edu.cn

ABSTRACT

Manipulating the properties of the isofrequency contours (IFCs) of materials provides a powerful means of controlling the interaction between light and matter. Hyperbolic metamaterials (HMMs), an important class of artificial anisotropic materials with hyperbolic IFCs, have been intensively investigated. Because of their open dispersion curves, HMMs support propagating high-k modes and possess an enhanced photonic density of states. As a result, HMMs can be utilized to realize hyperlenses breaking the diffraction limit, metacavity lasers with subwavelength scale, high-sensitivity sensors, long-range energy transfer, and so on. Aimed at those who are about to enter this burgeoning and rapidly developing research field, this tutorial article not only introduces the basic physical properties of HMMs but also discusses dispersion manipulation in HMMs and HMM-based structures such as hypercrystals. Both theoretical methods and experimental platforms are detailed. Finally, some potential applications associated with hyperbolic dispersion are introduced.

I. INTRODUCTION

Recently, hyperbolic metamaterials (HMMs),[1–4] also known as indefinite media,[5,6] have attracted considerable interest. An HMM is a special type of anisotropic metamaterial whose isofrequency contour (IFC) takes the form of an open hyperboloid because the principal components of its electric or magnetic tensor have opposite signs.[7–10] The unusual nature of the IFC enables HMMs to be used for controlling electromagnetic waves in new ways. By tuning the shape of the hyperbolic dispersion, the propagation of light in HMMs may be flexibly controlled, producing all-angle negative refraction,[11–15] collimation,[16–20] splitting,[21–23] near-perfect absorption,[24–28] and abnormal scattering.[29–32] In contrast to the closed IFC of normal materials (such as air), the hyperboloid IFC in HMMs is open and large wave-vectors can be supported.[33–35] As a result, the optical density of states (DOS) in the HMM can be greatly increased, which has important consequences for strong enhancement of spontaneous emission (SE)[36–40] and Cherenkov emission with low energy electrons.[41–44] In addition, because evanescent waves with large wave-vectors in normal materials can become propagating waves in this strongly anisotropic medium, HMMs can be used for super-resolution imaging that beats the diffraction limit.[22,45–51] Recent work has demonstrated that HMMs can overcome the short-range limitation of near-field coupling and produce long-range dipole–dipole interactions.[52–55] Specifically, with the aid of HMMs for dipole–quadrupole interactions, long-range electromagnetic induced transparency has been theoretically proposed and experimentally demonstrated.[56]

Both natural materials and artificial structures that exhibit hyperbolic dispersion have been discovered. Owing to the excitation of phonon polaritons, certain natural materials [such as graphite, SiC, Bi_2Se_3, and hexagonal boron nitride (h-BN)] can possess hyperbolic dispersion in the infrared and visible ranges.[57–69] Artificial structures with subwavelength unit cells can also display hyperbolic dispersion.[70–73] The use of effective medium theory (EMT) has led to the construction of HMMs in different spectral ranges, with architectures including metal–dielectric structures,[74–76] metallic nanowire structures,[77–81] multilayer fishnets,[82] circuit systems,[18,19,22,56,83,84] and uniaxial metasurfaces.[85–88] Beyond EMT, hyperbolic dispersion can be manipulated through the nonlocal effects of surface waves on metasurfaces.[89–93]

Very recently, composite structures containing HMMs, such as cavities and lasers containing HMMs,[94–96] hypercrystals,[97,98] and waveguides containing HMMs,[99–103] have been developed utilizing unusual properties for controlling electromagnetic waves. For example, unlike conventional cavities, HMM-based cavities exhibit size-independent resonance frequencies and anomalous scaling. These properties enable the construction of subwavelength cavities. A waveguide composed of HMMs is capable of strongly confining the guided modes and can be used for rainbow trapping.[104,105] Metasurfaces with HMMs have been utilized for asymmetric transmission[106] and high-efficiency wave-front manipulation.[107] The scope of research involving HMMs has been extended to actively controlled structures with graphene and VO_2,[108–110] in which hyperbolic dispersion and associated properties can be actively tuned by changing an external field. Many additional interesting phenomena and properties have been discovered in active HMMs, including the enhanced nonlinear effect,[111–113] enhanced magneto-optical effect,[114–117] and topological edge states.[118,119] The above-mentioned properties and applications have also been extended from photonics to acoustic[120–124] and elastic waves.[125–127]

Although HMMs can be realized in many systems, in this tutorial, we focus primarily on two implementations. The first system is based on microwave circuits, in which the unusual physical properties of HMMs can be clearly observed. The second involves multilayered structures that produce HMMs at visible wavelengths. Numerous optical devices, such as perfect optical absorbers and high-sensitivity biosensors, can be designed using these types of multilayered structures.

II. BASIC PHYSICS OF HYPERBOLIC METAMATERIALS

A. Physical properties

1. Dispersion relations of the anisotropic materials

The electromagnetic response of materials depends on their permittivity and permeability.[128–133] The relative permittivity or permeability tensor of an anisotropic material is given by

$$\hat{\varepsilon} = \begin{pmatrix} \varepsilon_{xx} & 0 & 0 \\ 0 & \varepsilon_{yy} & 0 \\ 0 & 0 & \varepsilon_{zz} \end{pmatrix} \quad \text{or} \quad \hat{\mu} = \begin{pmatrix} \mu_{xx} & 0 & 0 \\ 0 & \mu_{yy} & 0 \\ 0 & 0 & \mu_{zz} \end{pmatrix}. \tag{1}$$

For electric (magnetic) biaxial media, $\varepsilon_{xx} \neq \varepsilon_{yy} \neq \varepsilon_{zz}$ ($\mu_{xx} \neq \mu_{yy} \neq \mu_{zz}$). However, for electric (magnetic) uniaxial media, $\varepsilon_{xx} = \varepsilon_{yy} = \varepsilon_{//}$, $\varepsilon_{zz} = \varepsilon_{\perp}$ ($\mu_{xx} = \mu_{yy} = \mu_{//}$, $\mu_{zz} = \mu_{\perp}$), the subscripts $\perp$ and // indicate that the components are perpendicular and parallel to the xy plane, respectively, and the optical axis is along the z direction. Without considering nonlocal effects and electromagnetic coupling, the dispersion relation of a material can be determined by substituting Eq. (1) into Maxwell's equations,

$$\nabla \times \vec{E} = -\frac{\partial \vec{B}}{\partial t}, \tag{2}$$

$$\nabla \times \vec{H} = \frac{\partial \vec{D}}{\partial t}, \tag{3}$$

where $\vec{E}$, $\vec{B}$, $\vec{H}$, and $\vec{D}$ denote the electric field, magnetic induction, magnetic field, and electric displacement, respectively. Assume that the electric and magnetic fields are described by $\vec{E} = \vec{E}_0 e^{i(\omega t - \vec{k}\cdot\vec{r})}$ and $\vec{H} = \vec{H}_0 e^{i(\omega t - \vec{k}\cdot\vec{r})}$, respectively, where $\vec{k}$ is the wave-vector. Let us now consider electric uniaxial media. Supposing that $\mu_{//} = \mu_{\perp} = 1$, the wave equation for the electric field in a uniaxial medium can be written as

$$\begin{aligned} k_x(k_xE_x + k_yE_y + k_zE_z) &= (k^2 - k_0^2\varepsilon_{//})E_x \\ k_y(k_xE_x + k_yE_y + k_zE_z) &= (k^2 - k_0^2\varepsilon_{//})E_y \\ k_z(k_xE_x + k_yE_y + k_zE_z) &= (k^2 - k_0^2\varepsilon_{\perp})E_z \end{aligned}, \tag{4}$$

where k_x, k_y, and k_z denote the x, y, and z components of the wave-vector, k_0 is the wave-vector in free space, and $k^2 = k_x^2 + k_y^2 + k_z^2$. Solving the system of equations in Eq. (4) allows the dispersion relation to be derived[1–4]

$$(k_x^2 + k_y^2 + k_z^2 - \varepsilon_{//}k_0^2)\left(\frac{k_x^2 + k_y^2}{\varepsilon_{\perp}} + \frac{k_z^2}{\varepsilon_{//}} - k_0^2\right) = 0. \tag{5}$$

The first term in brackets in Eq. (5) describes a transverse-electric (TE) polarized wave in which the electric field is in the xy plane,[2] perpendicular to the optical axis ($\hat{z}\cdot\vec{E} = 0$). This TE mode corresponds to an ordinary wave. The second term describes a transverse-magnetic (TM) polarized wave in which the magnetic field is in the xy plane ($\hat{z}\cdot\vec{H} = 0$). This TM mode corresponds to an extraordinary wave. When $\varepsilon_{//} > 0$, $\varepsilon_{\perp} < 0$, TE and TM modes can coexist. In this case, the IFC of the TE mode takes the form of a sphere. However, the IFC of the TM mode corresponds to a twofold hyperboloid, where the two hyperbolic surfaces are oriented along the optical axis, as shown in Fig. 1(a). The corresponding material is called a dielectric-type or Type I HMM. In the second case, where $\varepsilon_{//} < 0$, $\varepsilon_{\perp} > 0$, the TE mode is absent. For the TM mode, the IFC has the form of a onefold hyperboloid, as shown in Fig. 1(b); this type of electric HMM is called a metal-type or Type II HMM.

According to the duality principle of electromagnetic fields, the corresponding dispersion relation for a magnetic medium

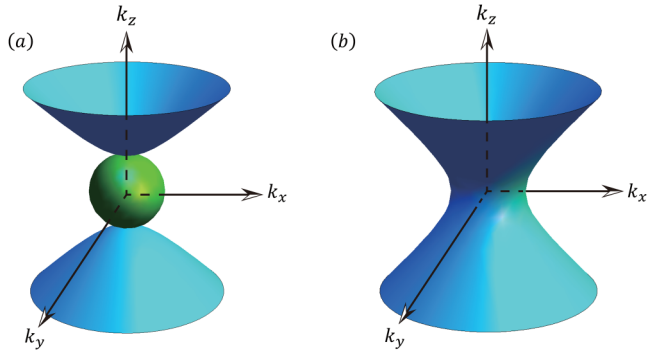

FIG. 1. The blue twofold hyperboloid and the green sphere in (a) denote the IFCs of TM and TE modes for a dielectric-type HMM, respectively. The blue onefold hyperboloid in (b) denotes the IFC of TM modes for a metal-type HMM.

$(\mu_{//}\mu_{\perp} < 0)$ with isotropic permittivity $\varepsilon_{//} = \varepsilon_{\perp} = \varepsilon$ may be written as

$$(k_x^2 + k_y^2 + k_z^2 - \varepsilon\mu_{//}k_0^2)\left(\frac{k_x^2 + k_y^2}{\mu_{\perp}} + \frac{k_z^2}{\mu_{//}} - \varepsilon k_0^2\right) = 0. \quad (6)$$

In Eq. (6), the dispersion relations of the TM and TE polarized waves are described by the expressions in the first and second brackets, respectively. Comparing Eq. (5) with Eq. (6), it may be seen that similar IFCs to those shown in Fig. 1 are also obtained for magnetic HMMs. Both dielectric-type and metal-type HMMs can be effectively controlled by tuning the signs of the permittivity and permeability.

2. Enhanced spontaneous emission

For normal materials with closed IFCs (such as air), the allowed modes are limited. However, the IFCs of HMMs take the form of open hyperboloids. As a result, modes with large wave-vectors can be supported, which leads to an enhancement of the optical DOS.[38,134–136] When the frequency increases from ω to $\omega + \delta\omega$, the number of allowed optical modes in the wave-vector interval $\delta k_x \delta k_y \delta k_z$ is

$$\delta N = (V\delta k_x \delta k_y \delta k_z)/(2\pi)^3, \quad (7)$$

where V denotes the volume of the material. Take an isotropic nonmagnetic material as an example. The IFC is a closed sphere. For the infinitely thin spherical shell between k and $k + \delta k$, $\delta k_x \delta k_y \delta k_z = 4\pi k^2 \delta k$. In this case, the number of modes is found to be[133]

$$\delta N = (V\varepsilon^{3/2}\omega^2)/2\pi^2 c^3 \delta\omega, \quad (8)$$

where ε is the permittivity and c is the velocity of light in vacuum. From Eq. (8), we see that the optical DOS in a material with a spherical IFC has a finite value because the closed IFC is integrable. Similarly, the optical DOS in a material with a closed elliptical IFC also takes a finite value. However, for an open IFC, the volume integral of the shell from k to $k + \delta k$ diverges and the optical DOS is infinite, $\delta N(k) \to \infty$. Figure 2 shows examples of closed and open IFCs. Comparing Fig. 2(a) with Fig. 2(b), it is apparent that the HMM, with an open IFC, has a diverging shell volume in the lossless limit, which implies that the HMM can support an infinite optical DOS. Therefore, materials with open IFCs provide powerful means for controlling the interaction between light and matter, as we will show later.

Spontaneous emission (SE), a typical quantum optical phenomenon, plays an important role in light-emitting devices. The emission rate can be expressed as[136–138]

$$\Gamma_T = \frac{1}{\tau} = \frac{2\pi}{\hbar}\left|\langle f|\vec{d}\cdot\vec{E}|i\rangle\right|^2 \rho(\hbar\omega), \quad (9)$$

where τ is the lifetime of the SE, which depends directly on the optical DOS $\rho(\hbar\omega)$.[139] $\langle f|\vec{d}\cdot\vec{E}|i\rangle$ is the transition matrix element. The enhancement of SE can be represented by the Purcell factor

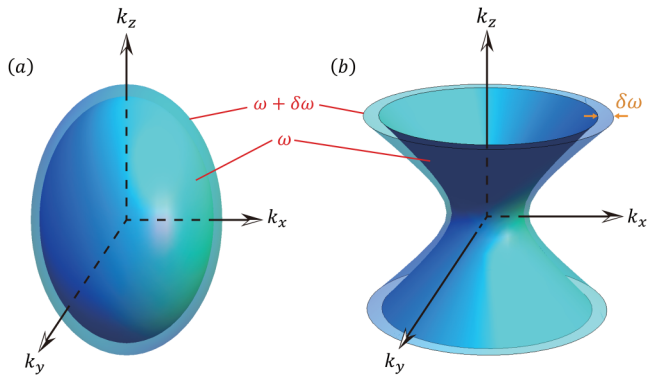

FIG. 2. The variation of IFCs for (a) a closed ellipsoid and (b) an open hyperboloid when the frequency increases from ω to $\omega + \delta\omega$.

$F_p = \Gamma_T/\Gamma_0$, where Γ_0 is the spontaneous emission rate in vacuum.[140] From Eq. (9), it is evident that F_p depends strongly on the optical DOS of the surrounding medium. The optical DOS $\rho(\hbar\omega)$ is equal to $\sum_k \hbar\delta(\omega_k - \omega)$, which can effectively be tuned by changing the shell volume enclosed by the corresponding IFC.[1] Therefore, along with the topological transition of dispersion from a closed IFC to an open IFC, the SE in a medium will be significantly enhanced because the optical DOS will gradually diverge.

In 2011, the Purcell factor of an electric dipole with a finite volume, such as a quantum dot, in an HMM was studied theoretically.[141] The radiative lifetime is

$$\frac{1}{\tau_\alpha} = -\frac{8\pi d^2 q_0^2}{\hbar}\int \frac{d^3k}{(2\pi)^3}\,\mathrm{Im}\,G_{k,\alpha\alpha}\Phi_k^2, \quad \alpha = x, y, \text{ or } z, \quad (10)$$

where $q_0 = \omega/c$ is the wave-vector in vacuum and d is the effective matrix element of the dipole moment. Φ_k denotes the distribution of the emitter polarization and G_k is the Green's function in k space. The lifetimes $\tau_x = \tau_y$ and τ_z describe the decay of the source when it is initially polarized in the $x - y$ plane and along the z axis, respectively.[141] The larger the Purcell factor, the faster the electrons relax from higher states to lower ones. In consequence, the intensity of the radiated light decays faster and the radiative lifetime is shorter. Reducing the radiation lifetime is of great significance for improving fluorescence efficiency.[142–145] The permittivity and permeability of the HMM are assumed to be[141]

$$\varepsilon_\perp(\omega) = \varepsilon_\perp^0 + \frac{\Gamma_0}{\omega_0 - \omega - i\Gamma}, \quad \varepsilon_{//} = 1, \quad \mu = 1. \quad (11)$$

The dependence of $\varepsilon_\perp$ on the normalized frequency $(\omega_0 - \omega)/\Gamma_0$ is shown in Fig. 3(a). The red, orange, yellow, green, cyan, and blue lines correspond to $\Gamma/\Gamma_0 = 0.01,\ 0.015,\ 0.02,\ 0.03,\ 0.05$, and 0.1, respectively. The real and imaginary parts of $\varepsilon_\perp$ are marked by solid and dashed lines. The sign of $\varepsilon_\perp$ depends on the sign of the normalized frequency. When $\varepsilon_\perp$ and $\varepsilon_{//}$ have the same sign, the IFC of the system corresponds to elliptical dispersion; opposite signs produce hyperbolic dispersion. The Purcell factors as a function of

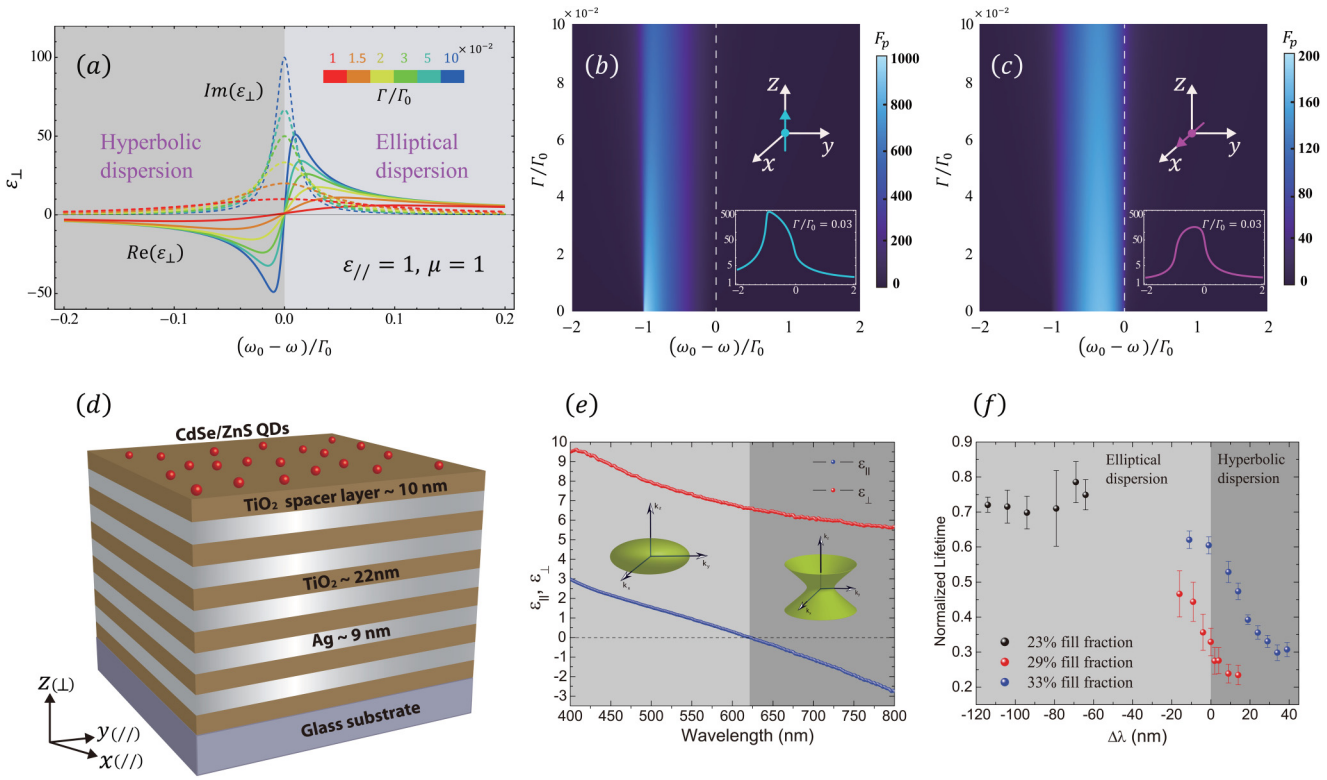

FIG. 3. (a) Perpendicular component of permittivity as a function of the normalized frequency. The solid and dashed lines correspond to the real and imaginary parts, respectively. (b) The Purcell factor as a function of $(\omega_0 - \omega)/\Gamma_0$ and Γ/Γ_0 when a dipole source directed along z is placed into the material. (c) Similar to (b), but with the dipole source oriented along the x direction. Reproduced with permission from Poddubny *et al.*, Phys. Rev. A **84**, 023807 (2011). Copyright 2011 American Physical Society. (d) Schematic of quantum dots on the surface of a multilayered HMM structure. (e) Effective perpendicular and parallel components of permittivity for the multilayered structure. Across 400 nm wavelength, the IFC changes from a closed ellipsoid to an open hyperboloid. (f) The measured radiative lifetime of the quantum dots on the surface of the multilayered structure. Reproduced with permission from Krishnamoorthy *et al.*, Science **336**, 205 (2012). Copyright 2012 American Association for the Advancement of Science.

$(\omega_0 - \omega)/\Gamma_0$ and Γ/Γ_0 are shown in Figs. 3(b) and 3(c) for dipoles oriented along z and x, indicated by the cyan arrow and the pink arrow, respectively. The figures demonstrate that the Purcell factor is greatly enhanced in the hyperbolic region but not in the elliptical region. In order to show this feature more clearly, the dependence of the Purcell factor on the normalized frequency is plotted for a fixed value of $\Gamma/\Gamma_0 = 0.03$ in the insets of Figs. 3(b) and 3(c).

The increase in spontaneous emission rates of emitters has been observed.[38] In this experiment, CdSe/ZnS colloidal quantum dots were placed in the near field of an HMM formed of a multilayered structure of silver and titanium dioxide (TiO_2) thin films, as illustrated in Fig. 3(d). Owing to the dispersion of the silver, the effective parameters are frequency dependent. Figure 3(e) shows that as the wavelength increases, the multilayered structure undergoes a topological transition from a closed IFC to an open IFC.[38] This transition causes a significant decrease in the spontaneous emission lifetime of the quantum dots, as depicted in Fig. 3(f). The decrease in lifetime is caused by the increased optical DOS that results from the topological transition of the IFC from a closed ellipsoid to an open hyperboloid.[38]

The radiation patterns produced by point sources in materials can visually represent the IFC of those materials. The theory of Green's functions may be used to obtain the dipole emission in a material.[146] The theoretical emission patterns of HMMs were calculated in Ref. 147. The two dimensional (2D) IFC, in which only the relationship between k_x and k_z need to be studied, was used to analyze the light emission. The 2D IFC of an isotropic material ($\varepsilon = 1$, $\mu = 1$) is shown in Fig. 4(a), with the group velocity (density of energy flow) marked by green arrows. Figure 4(e) presents the calculated radiation pattern for a dipole source placed in the material. Assuming that $\mu_y = 1$, the 2D IFCs for three different anisotropic materials with elliptical ($\varepsilon = 1$, $\mu_x = 1$, $\mu_z = 2$), hyperbolic ($\varepsilon = 1$, $\mu_x = -2$, $\mu_z = 1$), and linear-crossing ($\varepsilon \to 0$, $\mu_x = -2$, $\mu_z = 1$) dispersions are shown in Figs. 4(b)–4(d), respectively. Comparing Fig. 4(d) with Fig. 4(c), it can be seen that a topological transition of the IFC will happen once $\varepsilon > 0$, $\mu_x\mu_z < 0$. Moreover, the IFC takes the form of two crossing straight lines when the parameters become $\varepsilon \to 0$, $\mu_x\mu_z < 0$.[22] The calculated emission patterns for the same parameters, given in Figs. 4(e)–4(h), coincide well with the corresponding IFCs in Figs. 4(a)–4(d).

For example, in the case of elliptical dispersion [Fig. 4(b)], light can propagate in all in-plane directions [Fig. 4(f)]. However, in the case with open hyperbolic dispersion [Fig. 4(c)], light can only propagate within a certain range of angles [Fig. 4(g)], and the field perpendicular to the hyperbolic asymptotes is much stronger than elsewhere because of the larger optical DOS. The effect is particularly pronounced in the case of linear-crossing dispersion, where the light is collimated and only propagates in two directions.[22] Therefore, it can be seen that the light emission patterns can be effectively controlled by the IFCs of the materials. In experiments, emission patterns can be measured when a point source is placed inside the structures.[19,83,84,148,149] The calculated field distributions as shown in Figs. 4(e)–4(h) can be used to determine the IFC of materials by using the Fourier transform.[150,151]

3. Abnormal refraction, reflection, and scattering

Metamaterials, artificial materials composed of subwavelength unit cells, provide a powerful platform for manipulating the propagation of light.[128–133] The existence of counterintuitive negative refraction and superlensing beyond the diffraction limit was initially confirmed in left-handed metamaterials.[128,129] Numerous other intriguing optical phenomena have been discovered, such as cloaking using transform optics,[130] optical tunneling,[152] and light trapping.[153–155] In recent years, the unprecedented ability of HMMs to tune electromagnetic waves has allowed the implementation of unusual effects, including negative refraction,[11–15] near-perfect absorption,[24–28] abnormal scattering,[29–32] and directional propagation.[22] Unlike left-handed metamaterials and metamaterials with complex electromagnetic distributions, HMMs are very easy to produce so long as the principal components of the electromagnetic parameters have opposite signs.[1–4] Either positive or negative refraction of light can exist in HMMs, and the IFCs of materials can be used to analyze their abnormal optical properties. To illustrate this point clearly, four types of magnetic HMMs are shown in Fig. 5. All four have the normal dispersion characteristics $\varepsilon(\omega+\delta\omega)>\varepsilon(\omega)$, $\mu(\omega+\delta\omega)>\mu(\omega)$, where $\delta\omega$ denotes an infinitesimal increase in frequency, meaning that the permittivity and permeability will increase as the frequency increases. The IFCs of the four HMMs are shown in blue in Figs. 5(a)–5(d), where the solid and dashed lines correspond to the values at the frequencies ω and $\omega+\delta\omega$, respectively. For comparison, the IFCs of air are also shown in red. The light is incident from air (the lower part) to the HMM (the upper part) at an oblique angle of 20°, marked by the red arrow denoting the wave-vector k_1. Using the law of conservation of tangential wave-vectors and the law of causality, the wave-vector k_2 and the Poynting vector S in the HMM can be determined as shown in the figures. We assume that $\varepsilon_x=\varepsilon_z=1$, $\mu_y=1$. The first case (HMM1: $\varepsilon_y>0$, $\mu_x>0$, $\mu_z<0$) belongs to the dielectric type of HMMs, in which negative refraction will

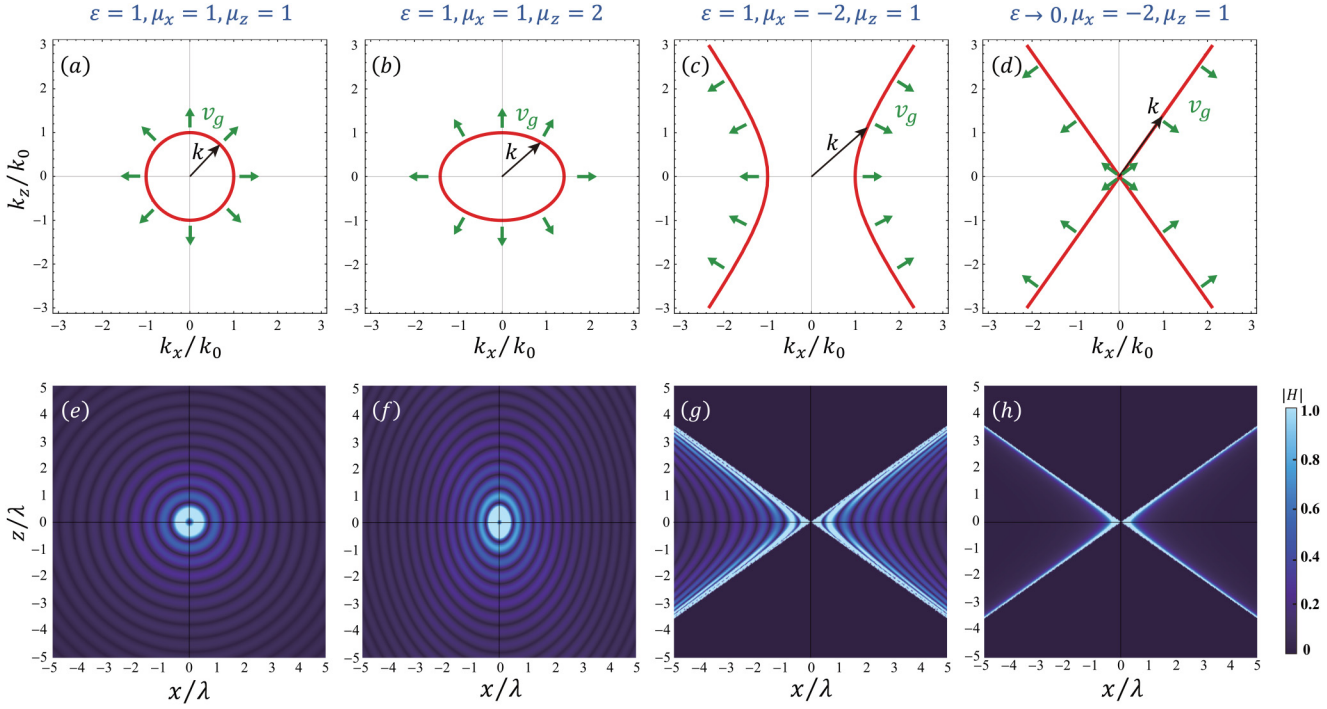

FIG. 4. IFCs (upper row) and the corresponding in-plane magnetic field $|H|$ distributions (lower row) for various types of materials. The green arrows in the upper row denote group velocity. (a) $\mu_x=\mu_z$, corresponding to an isotropic material. (b)–(d) $\mu_x\neq\mu_z$, corresponding to elliptical, hyperbolic, and linear-crossing anisotropic materials, respectively.

occur. However, unlike the negative refraction of left-handed materials,[127,156] the directions of the wave-vector and the energy flow in HMMs form a certain angle rather being completely antiparallel, as shown in Fig. 5(e). The second case (HMM2: $\varepsilon_y < 0$, $\mu_x < 0$, $\mu_z > 0$) is also a dielectric-type HMM. This time, however, the dashed line is outside the solid line in Fig. 5(b), which means that the IFC expands with the increase in frequency. Therefore, the light incident on this HMM will undergo positive refraction, as seen in Fig. 5(f). HMM3 ($\varepsilon_y > 0$, $\mu_x < 0$, $\mu_z > 0$) and HMM4 ($\varepsilon_y < 0$, $\mu_x > 0$, $\mu_z < 0$) are metal-type HMMs. Positive and negative refraction, respectively, can occur in HMM3 and HMM4 only when the tangential wave-vector in air is greater than a critical value. If the incident angle is less than the critical angle, the incident wave will be totally reflected. In particular, in Figs. 5(g) and 5(h), the Goos–Hänchen (GH) shift associated with total reflection is positive in HMM3 and negative in HMM4. Refractive index sensing has recently been demonstrated by exploiting the singular phase of light associated with the enhanced GH shift in HMMs.[157–160]

In addition to anomalous refraction and reflection, HMMs can manipulate the scattering behavior of electromagnetic waves in novel ways.[30–32] For example, anomalously weak scattering can be achieved in HMMs based on Au–Si multilayers.[30] Scattering of the field depends on $\varepsilon_E/\varepsilon_B - 1$, where ε_E denotes the permittivity of the HMM in the direction of the electric field and ε_B is the permittivity of the surrounding medium. If the value of ε_E is close to that of ε_B, the scattering becomes very weak.[30] On the other hand, superscattering, induced by overlapping multiple discrete resonances of subwavelength objects, breaks the fundamental single-channel limit of the scattering cross section.[161] The hyperbolic dispersion of phonon polaritons within the two Reststrahlen bands of boron nitride allows overlapped multimode resonances to be realized in two frequency bands, leading to multifrequency superscattering.[31] What is more, in lossy HMMs, the scattering caused by radiative decay channels and the absorption caused by nonradiative decay channels can be effectively controlled.[28,142]

B. Realization ways of HMMs

1. Effective medium theory

Within an effective medium theory, the periodic arrangement of artificial structures with subwavelength unit-cell size can be regarded as an effective homogeneous medium, characterized by homogeneous macroscopic permittivity and permeability.[5,6,162] By designing suitable artificial structures such as metal/dielectric multilayers [Fig. 6(a)], metal nanowire arrays [Fig. 6(b)], multilayer fishnets [Fig. 6(c)], or microwave circuit systems loaded with lumped elements [Figs. 6(d) and 6(e)], HMMs can be conveniently engineered.[1–4] Generally, the Maxwell–Garnett approximation of EMT is valid when the wavelength of the incident wave is much larger than the unit-cell size. EMT is a quasistatic approximation and hence may be invalid when nonlocal optical effects exist in the system.[163–168] For example, the validity of the approximation may be affected when surface plasmon polaritons (SPPs) are excited on the surface of a metal layer.[163,165] Nevertheless, in layered metal–dielectric HMMs, the extraordinary wave is formed by the coupling of the individual surface plasmons at each metal–dielectric interface. If the wavelength of the incident wave is much larger than the periodic length of the metal–dielectric multilayer, EMT still works well even though SPPs are excited.[169]

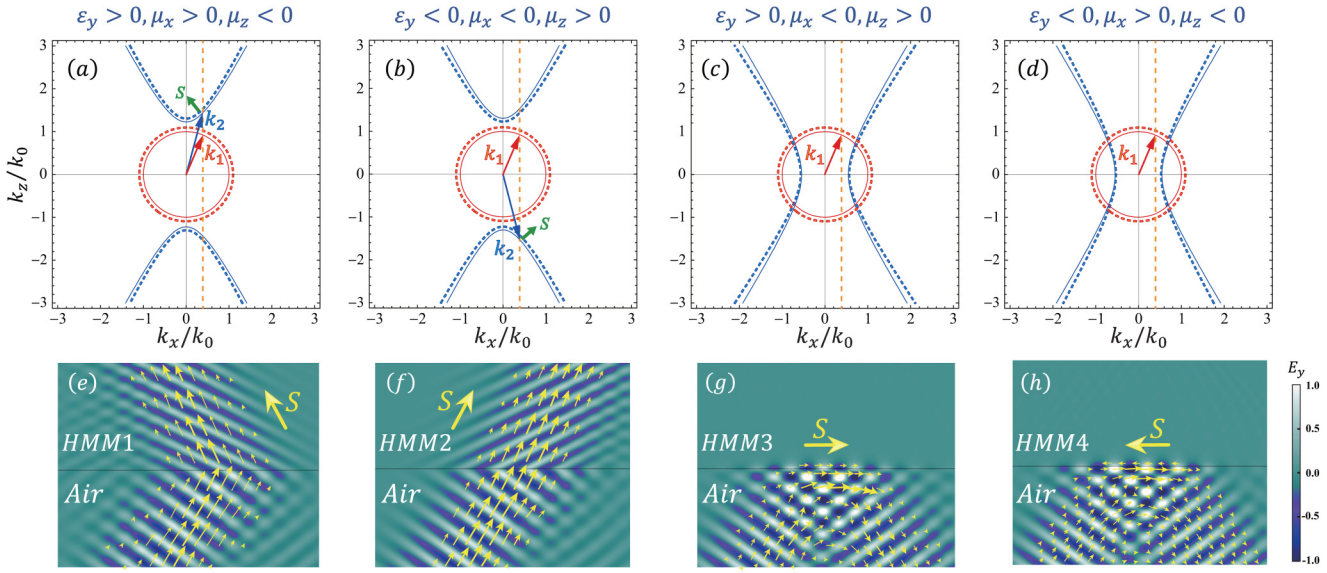

FIG. 5. IFCs (upper row) and the corresponding electric field E_y distributions (lower row) for four different examples of HMMs. The red and blue arrows in the upper row denote the wave-vectors in air and the HMM, respectively. The green arrows in the upper row denote the group velocity in the HMM. In (e)–(h), the light is incident from air onto the HMM, and the yellow arrow denotes the group velocity in the HMM.

In the visible range, both metal/dielectric multilayers and metal nanowire arrays may be used to create electric HMMs with anisotropic permittivity, according to EMT. Specifically, the effective parameters of the metal/dielectric multilayer structure in Fig. 6(a) can be expressed by[74]

$$\varepsilon_{//} = p\varepsilon_m + (1-p)\varepsilon_d, \quad \varepsilon_\perp = \frac{\varepsilon_m\varepsilon_d}{p\varepsilon_d + (1-p)\varepsilon_m}, \tag{12}$$

where $p = t_m/(t_m + t_d)$ is the filling ratio of the metal layer. ε_m (ε_d) is the permittivity and t_m (t_d) is the thickness of the metal (dielectric) layer. Once the parameters are tuned to satisfy the condition $\varepsilon_{//}\varepsilon_\perp < 0$, the metal/dielectric multilayer structure can be considered as an electric HMM. Metal nanowire arrays, as in Fig. 6(b), can also be used to construct electric HMMs, with effective permittivity given by[170]

$$\varepsilon_{//} = \frac{[(1+p)\varepsilon_m + (1-p)\varepsilon_d]\varepsilon_d}{(1-p)\varepsilon_m + (1+p)\varepsilon_d}, \quad \varepsilon_\perp = p\varepsilon_m + (1-p)\varepsilon_d, \tag{13}$$

where the filling ratio of the metal wires in the array is $p = A/A_0$. A and A_0 are the cross-sectional areas of the metal wires and the host material, respectively. Again, the signs of effective $\varepsilon_{//}$ and $\varepsilon_\perp$ can be tuned by changing the structural parameters.[51]

In addition to electric HMMs, magnetic HMMs with anisotropic permeability have recently attracted considerable attention.[7–10,22,56] For the multilayer fishnet metamaterial composed of metal and dielectric layers shown in Fig. 6(c), both the permittivity and the permeability can be tuned by changing the structural parameters or choosing a different wavelength.[7] In Ref. 7, the real part of $\varepsilon_{//}$ ($\varepsilon_\perp$) is positive (negative) at 1310 nm. In this case, the condition that $\varepsilon_{//}\varepsilon_\perp < 0$ is satisfied and the multilayer fishnet corresponds to an electric HMM. However, at a wavelength of 1530 nm, the condition $\mu_{//}\mu_\perp < 0$ is satisfied and a magnetic HMM is realized.[7] Alternatively, magnetic HMMs can be easily produced using circuit-based metamaterials in the microwave regime.[22,56] In the circuit system, the longitudinal components of the electric and magnetic fields are much smaller than the transverse components. Therefore, the resulting mode is called a quasitransverse electromagnetic (TEM) wave.[171,172] In the circuit-based system, the relationship between the electric and magnetic fields can be easily mapped using the relationship between voltage and current in the circuit.[171,172] As a result, the electromagnetic response is equivalent to the circuit parameters. In Fig. 6(d), the impedance and admittance of the circuit are represented by Z and Y, respectively. The direction of the magnetic field produced by the current can be determined from Ampere's law, as shown in Fig. 6(d). By mapping the circuit equation (telegraph equation) to Maxwell's equations, the relationship between circuit and electromagnetic parameters can be described by

$$Z = i\omega\mu, \quad Y = i\omega\varepsilon. \tag{14}$$

For a circuit without lumped elements, $Z = i\omega L_R$ and $Y = i\omega C_R$. When the microwave circuit is loaded with series

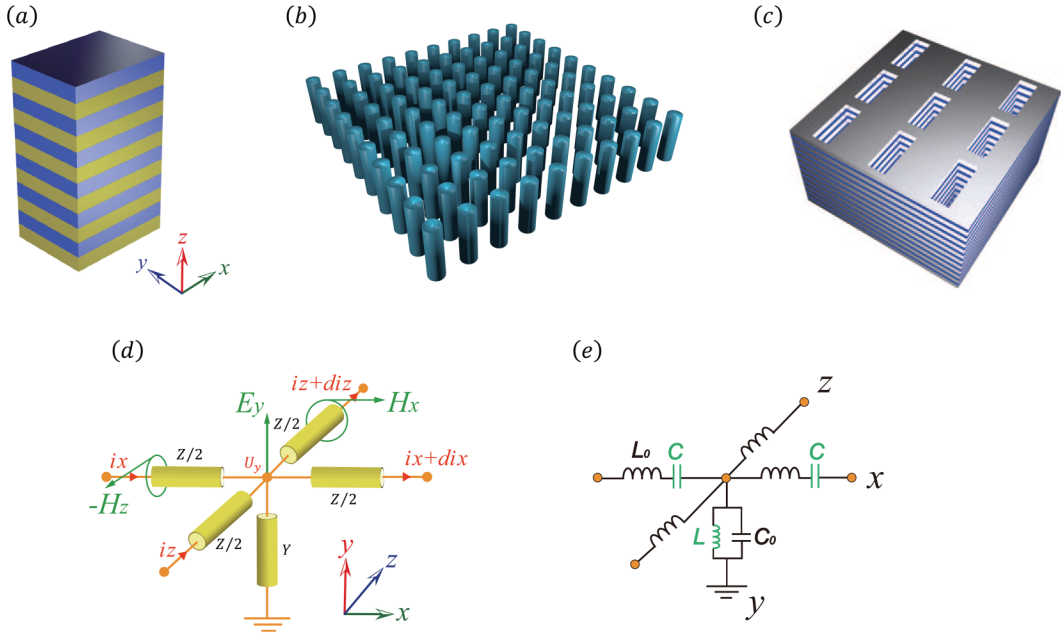

FIG. 6. Schematics of (a) metal/dielectric multilayer HMM, (b) metal nanowire HMM, and (c) multilayer fishnet HMM in the frequency range from THz to UV. Reproduced with permission from Poddubny *et al.*, Nat. Photon. **7**, 948 (2013). Copyright 2013 Springer Nature. (d) and (e) Circuit-based HMM in the microwave regime.

lumped capacitors C_L and shunted lumped inductors L_L,

$$Z = i\omega L_R + \frac{1}{i\omega C_L}, \quad Y = i\omega C_R + \frac{1}{i\omega L_L}. \tag{15}$$

The effective electromagnetic parameters of the circuit with lumped elements then become

$$\mu = i\omega L_R - \frac{1}{\omega^2 C_L}, \quad \varepsilon = C_R - \frac{1}{\omega^2 L_L}. \tag{16}$$

From Eq. (16), it can be seen that the effective permittivity and permeability of the circuit system can be tuned using the lumped elements in the circuit. Figure 6(e) shows a simple effective circuit model for a circuit-based HMM. In this circuit model, capacitors are loaded in the x direction to realize anisotropic permeability, with $\mu_x = L_R/g\varepsilon_0$. In the long-wavelength limit, if the loss is not considered, the effective permittivity and permeability of 2D circuits can be written as[22]

$$\begin{aligned} \varepsilon &= (2C_R g - g/\omega^2 L_L d)/\varepsilon_0, \\ \mu_y &= (L_R/g - 1/\omega^2 C_L d)/\varepsilon_0, \end{aligned} \tag{17}$$

where g is the structure factor, which can be tuned through the thickness of the dielectric layer and the width of the metal strip, and d is the length of a unit cell. Equation (17) shows that μ_y and ε can be adjusted independently by changing L_L and C_L. By tuning the sign of μ_y from positive to negative, a topological transition of the IFC from closed elliptical to open hyperbolic dispersion can be generated.

2. Hyperbolic metasurfaces

Flatland optics with hyperbolic metasurfaces (HMSs), in which the hyperbolic dispersion can be manipulated with in-plane SPPs, is a hot research topic at present.[87,173,174] By choosing different frequencies for the surface wave, elliptical or hyperbolic IFCs can be obtained. A variety of HMSs have been proposed, which work over frequencies ranging from visible light to the microwave regime.[173–179] One important HMS architecture is the metal nanograting array, which can effectively manipulate SPPs in the near-field region as well as exhibiting hyperbolic dispersion.[14,175] A schematic of the metal/air grating is shown in Fig. 7(a). The corresponding IFCs at different frequencies are given in Fig. 7(b). Based on the IFCs, the positive refraction, collimation, and negative refraction for red, green, and blue light can be determined.[14] Moreover, by using the physical mechanism of spin–orbit coupling of evanescent waves,[180–184] the photonic spin Hall effect (in which photons with different circular polarizations travel in different directions) has been experimentally observed.[14] In addition to the metal nanograting array, HMSs can be created using an anisotropic conductivity layer, as shown in Fig. 7(d), in which a conductive layer is sandwiched between two media with permittivities ε_1 and ε_2, respectively.[89] The dispersive conductivity in different directions in the plane yoz is shown in Fig. 7(e). By changing the frequency, the imaginary parts of $\sigma_{//}$ and $\sigma_\perp$ can be effectively tuned. The cases $\mathrm{Im}(\sigma_\perp) > 0$, $\mathrm{Im}(\sigma_{//}) > 0$ and $\mathrm{Im}(\sigma_\perp) < 0$, $\mathrm{Im}(\sigma_{//}) < 0$ correspond to inductive (behaving as a metal sheet) and capacitive (behaving as a dielectric sheet) metasurfaces, respectively.[89] When both $\mathrm{Im}(\sigma_\perp)$ and $\mathrm{Im}(\sigma_{//})$ are negative, the IFCs of the surface plasmon are ellipses and the excited plasmon can propagate in all directions in the yoz plane. However, when one of $\mathrm{Im}(\sigma_\perp)$ and $\mathrm{Im}(\sigma_{//})$ is positive, the IFCs of the surface plasmon are hyperbolas. Moreover, two types of hyperbolic dispersion with different principal axes can be realized depending on whether $\mathrm{Im}(\sigma_\perp) > 0$, $\mathrm{Im}(\sigma_{//}) < 0$ or $\mathrm{Im}(\sigma_\perp) < 0$, $\mathrm{Im}(\sigma_{//}) > 0$. As a result, the emission patterns of a dipole embedded in this HMS can be controlled, as shown in Fig. 7(f). In addition, an HMS based on the conductivity tensor that utilizes an array of graphene strips has been proposed.[86–88] In this actively controlled structure, a topological transition of the IFC from a closed ellipse to an open hyperbola can be achieved by adjusting the chemical potential of graphene (manipulation of dispersion using an external field will be introduced in detail in Sec. III A 3).

In the microwave regime, a magnetic HMS can be realized by manipulating the magnetic SPPs at the subwavelength scale.[10] In this type of HMS, arrays of coiling copper wires are fabricated on a dielectric substrate. As shown in Fig. 7(g), the double split ring resonator is the basic unit cell. By calculating the engine modes of the structure, the 3D dispersion relationship can be obtained and the IFCs at a fixed frequency can be determined. Looking at Fig. 7(h), as the frequency increases, a topological transition of the IFC will occur. In the microwave regime, the size and shape of the meta-atoms may be flexibly chosen in the fabrication process, and the electric and magnetic fields can be sensitively measured.[10] Using the near-field detection technology and Fourier transforms, the hyperbolic IFC of the HMS can be clearly observed in Fig. 7(f).

3. Natural hyperbolic media

The greatest advantage of artificial HMMs is that their structural parameters may be easily and flexibly controlled. However, in the high-frequency regime, the complex nanofabrication process means that artificial HMMs would have the limitations coming from the structural tolerances and the finite-size effect. Natural hyperbolic materials, such as graphite, SiC, Bi_2Se_3, MgB_2, and hexagonal boron nitride (h-BN), are an attractive alternative.[67,69] Many natural hyperbolic materials belong to the class of van der Waals (vdW) crystals (consisting of individual atomic planes bonded by weak vdW forces), and the polaritons in natural hyperbolic materials produce unprecedented control over light-matter interactions.[185,186] As a representative low-loss vdW material, h-BN supports both Type I and Type II hyperbolic phonon polaritons in two separated Reststrahlen bands in the midinfrared range.[65,187] The highly confined phonon polaritons in h-BN have properties analogous to SPPs. However, their ultrashort wavelengths and low loss compared with metal-based SPPs and graphene plasmons make them an excellent candidate for nanophotonics. The anisotropic permittivity of h-BN is shown in Fig. 8(a). When the signs of the out-of-plane relative permittivity ($\varepsilon_\perp$) and the in-plane relative permittivity ($\varepsilon_{//}$) are opposite, the polaritons possess an in-plane hyperbolic dispersion, with the IFCs being open hyperboloids. In the lower Reststrahlen band (760–825 cm^{-1}), $\varepsilon_\perp < 0$, $\varepsilon_{//} > 0$, and the phonon polaritons possess Type I

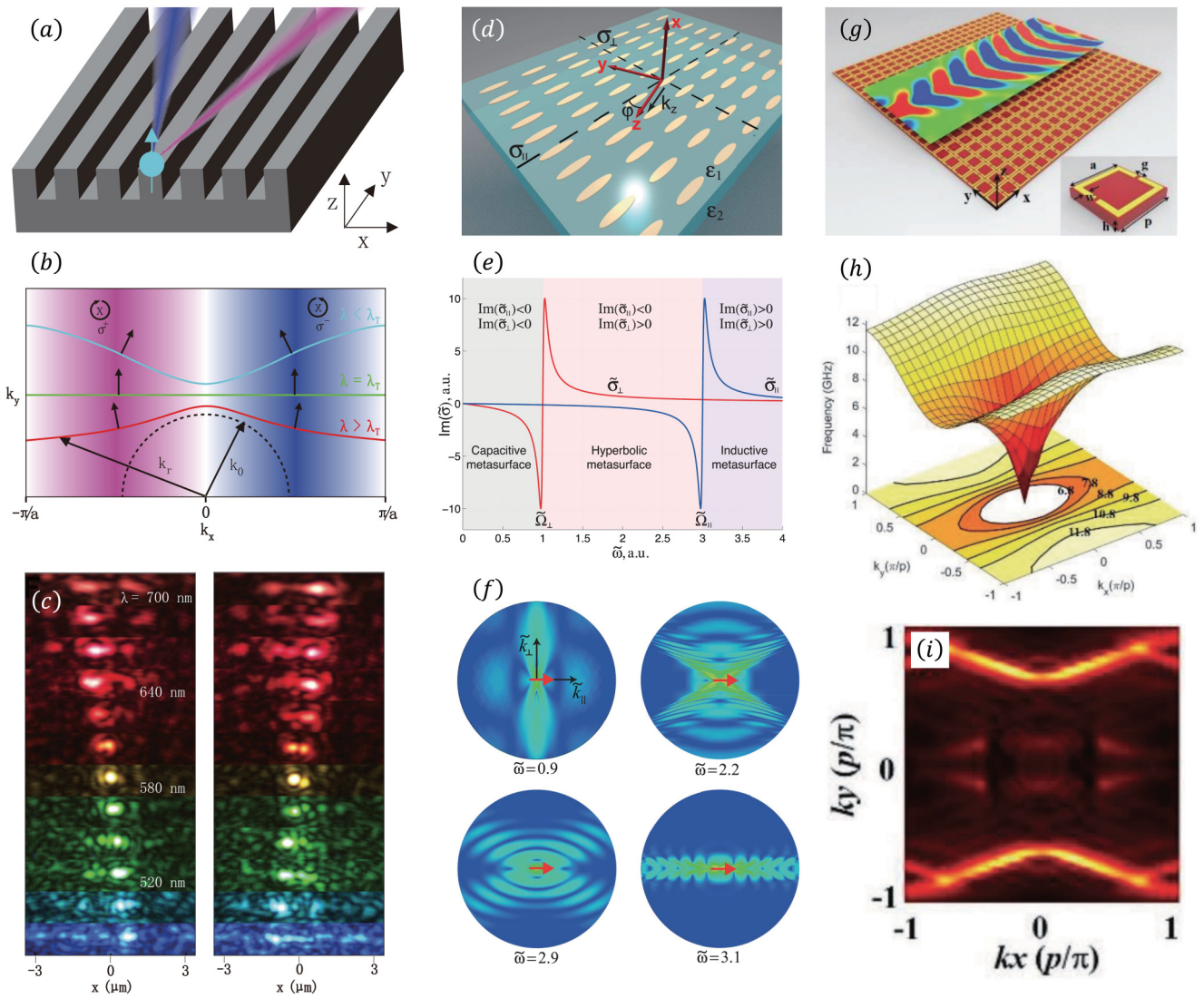

FIG. 7. HMS architectures. Metal/air grating: (a) schematic, (b) IFCs at different wavelengths, and (c) the photonic spin Hall effect. Reproduced with permission from High *et al.*, Nature **522**, 192 (2015). Copyright 2015 Springer Nature. Anisotropic conducting layer: (d) schematic, (e) the imaginary parts of the anisotropic conductivity, and (f) the electric field distributions at different frequencies. Reproduced with permission from Yermakov *et al.*, Phys. Rev. B **91**, 235423 (2015). Copyright 2015 American Physical Society. An array composed of split ring resonators: (g) schematic, (h) the 3D dispersion relationship and the 2D IFC, and (i) experimentally measured IFC. Reproduced with permission from Yang *et al.*, Adv. Sci. **5**, 1801495 (2018). Copyright 2018 Author(s), licensed under a Creative Commons Attribution-NonCommercial-NoDerivatives 4.0 International License.

hyperbolic dispersion. However, in the upper Reststrahlen band (1360–1610 cm^{-1}), $\varepsilon_{\perp} > 0$, $\varepsilon_{//} < 0$, and the phonon polaritons have Type II hyperbolic dispersion.[187] Special attention has been paid to the long lifetime and ultraslow propagating velocity of phonon polaritons as well as the subdiffraction imaging in h-BN.[58,188–190] The dispersion relation for the polariton modes in h-BN may be visualized using a false-color plot of the imaginary part of the reflectivity $\mathrm{Im}\, r_p(\omega - q)$, where q denotes the momentum, as shown in Fig. 8(b) for the hyperbolic photon-polariton modes in h-BN. A finite-thickness slab of h-BN can act as a multimode waveguide for the propagation of hyperbolic phonon polaritons. Due to the negative dispersion in the lower Reststrahlen band, the phonon polaritons in a layered h-BN slab can produce negative refraction.[58] The IFC of the hyperbolic phonon polaritons can be controlled by changing the frequency, and the propagation angle within the two spectral bands varies.

Subwavelength imaging in two separate spectral regions may also be achieved with h-BN. The imaging system is composed of an

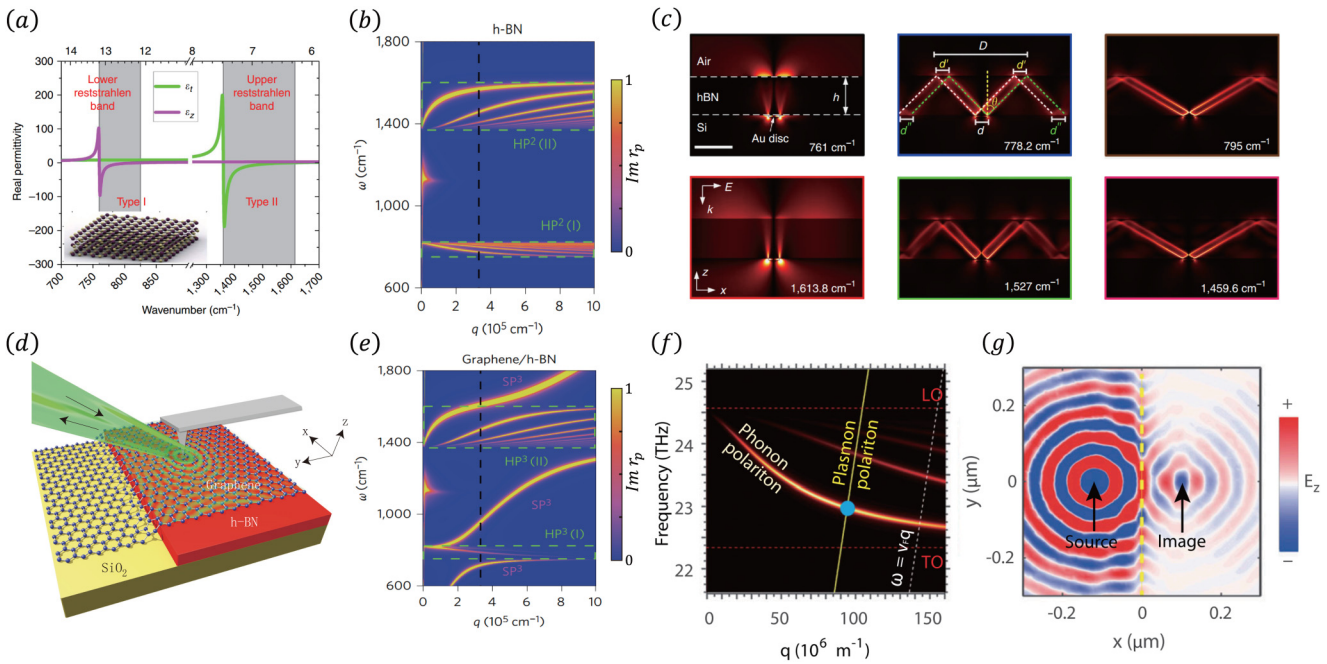

FIG. 8. Hyperbolic configurations of h-BN and graphene/h-BN. (a) Real parts of the permittivity tensor of h-BN. The two shaded regions are the Reststrahlen bands where $\varepsilon_{\perp}\varepsilon_{//} < 0$. Reproduced with permission from Caldwell *et al.*, Nat. Commun. **5**, 5221 (2014). Copyright 2014 Springer Nature. (b) Dispersion relations for the hyperbolic phonon polaritons in the h-BN layer with a thickness of 58 nm. (d) Schematic of a scattering-type scanning near-field optical microscope in a graphene/h-BN heterostructure, where the probe tip can be excited by a laser source. The scattered plasmons also are collected by the tip. (e) Dispersion relation for the phonon polaritons in a graphene/h-BN heterostructure. Reproduced with permission from Dai *et al.*, Nat. Nanotech. **10**, 682 (2015). Copyright 2015 Springer Nature. (c) Electric field distribution in h-BN. The directional angles of the hyperbolic polaritons can be tuned by choosing various frequencies. Reproduced with permission from Li *et al.*, Nat. Commun. **6**, 7507 (2015). Copyright 2015 Author(s), licensed under a Creative Commons Attribution-NonCommercial-NoDerivatives 4.0 International License. (f) Dispersion relation of the graphene/h-BN heterostructure with strong coupling between the plasmon and phonon polaritons. (g) Imaging of a point source in the graphene/h-BN heterostructure based on all-angle negative refraction. In the electric field distribution, the positions of the source and image are marked. Reproduced with permission from Lin *et al.*, Proc. Natl. Acad. Sci. U.S.A. **114**, 6717 (2017). Copyright 2017 National Academy of Sciences.

Si substrate, an Au disk, and an h-BN layer, as shown in Fig. 8(c). The polaritons are launched at the Au disk edges and propagate toward the h-BN layer. The electrical distribution of hyperbolic phonon polaritons at different frequencies is shown in Fig. 8(c). The propagation angle of the hyperbolic polaritons clearly depends on the frequency; the relationship $\tan\theta(\omega) = [D(\omega) - d]/2h$ can be quantitatively inferred from the reconstructed outline $D(\omega)$,[188] where h and d denote the thickness of h-BN layer and the width of gold stripe, respectively. The hyperbolic metasurface based on nanostructured vdW materials can be achieved by patterning a gating structure, where the h-BN ribbons are separated by air gaps.[191] In addition, anomalous internal reflection in a nanocone array composed of h-BN has been experimentally observed.[192] More broadly, the design idea of patterning new structures with h-BN can be extended to other vdW materials (such as MoS_2 or Bi_2Se_3) to manipulate hyperbolic phonon polaritons.

Although the two separated bands can realize hyperbolic phonon polaritons, the electrodynamic properties of h-BN are limited by the intrinsic crystal lattice. To overcome this limitation, heterostructures composed of graphene and h-BN have been proposed, which may allow the SPPs (coherent oscillations of the electron density) in graphene[193] and the hyperbolic phonon polaritons (atomic vibrations) in thin h-BN to be combined.[62,109,194–196] A schematic of a graphene/h-BN heterostructure is presented in Fig. 8(d). In this structure, the hybridized plasmon–phonon modes can effectively modulate the dispersion relations of the SPPs and phonon polaritons.[109,197] To explore the polaritonic response of the graphene/h-BN heterostructure, polariton interferometry (scattering-type scanning near-field optical microscopy) was performed in the experiment. The hyperbolic plasmon–phonon polariton possesses the combined virtues of graphene and h-BN, with a propagation length of 1.5–2.0 times greater than that of a hyperbolic phonon polariton in h-BN.[109] Figure 8(e) shows the dispersion relation of the graphene/h-BN heterostructure in Fig. 8(d). Comparing Fig. 8(e) with Fig. 8(b), we can see that the new collective modes, hyperbolic plasmon–phonon polaritons, can be controlled via the hybridization of SPPs and phonon polaritons. Importantly, the sign of the group velocity of the new hybrid modes also can be modulated using the strong mode coupling.[62] Figure 8(e) shows that the group velocity of the graphene plasmon polaritons is positive while that of the h-BN phonon polaritons is negative in the first Reststrahlen band of the h-BN. At a working

frequency of 22.96 THz, which corresponds to the blue point in Fig. 8(f), the wave-vectors of both types of polaritons are equal. Figure 8(g) presents the imaging of a point source in the graphene/h-BN heterostructure. Plasmons in graphene are excited by a dipole source in the left region (marked by the black arrow), and then couple to the polaritons in h-BN. As the group velocity in the h-BN is negative, an image of the source will occur in the right region due to the all-angle negative refraction at the interface (marked by the yellow dashed line). The existence of highly confined low-loss plasmons in graphene/h-BN heterostructures has been experimentally confirmed.[195]

Very recently, α-MoO_3 has been added to the growing list of vdW materials exhibiting polaritons.[63,198,199] In the midinfrared regime, thin flake α-MoO_3 can support hyperbolic phonon polaritons in different Reststrahlen bands. The α-MoO_3 lattice is composed of octahedron unit cells with nonequivalent Mo–O bonds along the three principal crystalline axes, as shown in Fig. 9(a).[198] The inset in Fig. 9(b) shows the unit cell of α-MoO_3, in which three different oxygen sites are indicated by O1–O3. In the midinfrared region, the optical response of α-MoO_3 is dominated by phonon absorption rather than electronic transitions, and the permittivity can be described by the Lorentz equation.[199] The permittivity tensor of this low-symmetry crystal can be written as $diag[\varepsilon_x, \varepsilon_y, \varepsilon_z]$ with $\varepsilon_x \neq \varepsilon_y \neq \varepsilon_z$, where at least one of the components is negative, as presented in Fig. 9(b). Three Reststrahlen bands are marked by pink, yellow, and blue shading. The signs of ε_i $(i = x, y, z)$ can be tuned by choosing different frequencies. The dispersion relation of α-MoO_3 can be calculated using the general Fresnel equation. From the special permittivity tensor, α-MoO_3 is expected to be a type of biaxial hyperbolic crystal. In the k-space of α-MoO_3, four conical singularities are connected, as illustrated in Fig. 9(c). In band 1 and band 2, one of the in-plane permittivity components $\varepsilon_i (i = x, y)$ is negative while the out-of-plane permittivity ε_z is positive, which induces in-plane hyperbolic dispersion

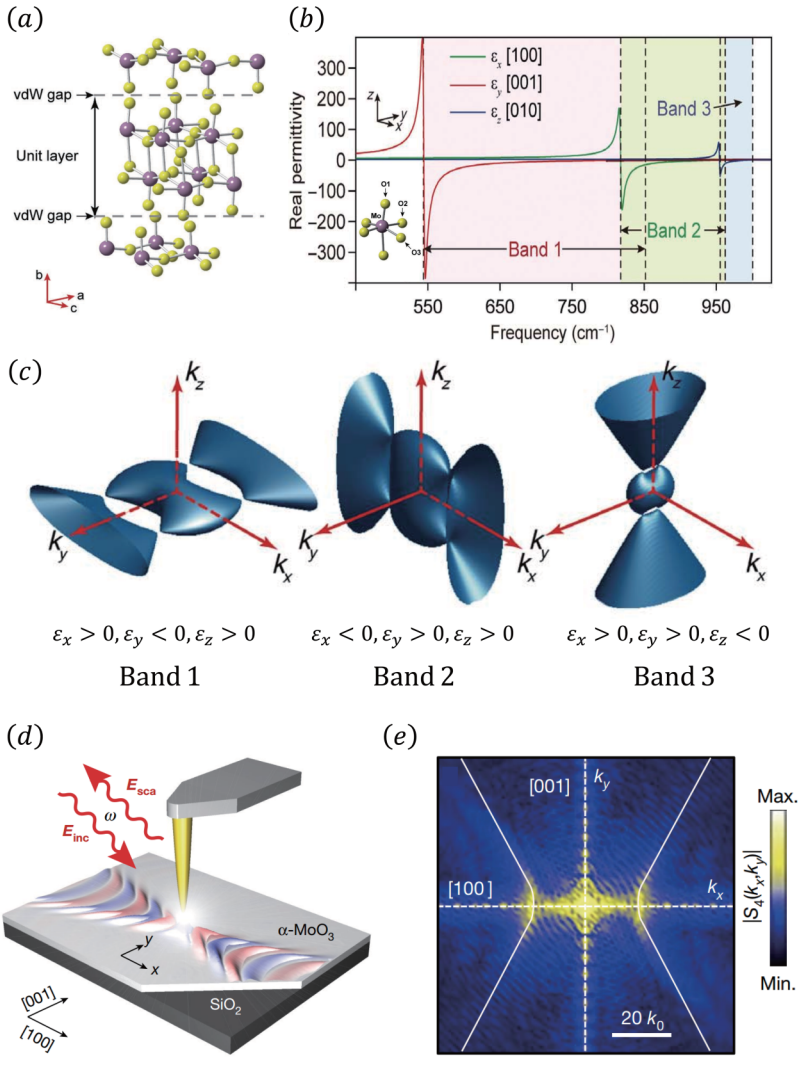

FIG. 9. The hyperbolic configuration of α-MoO_3. (a) Schematic of the α-MoO_3 crystal. Reproduced with permission from Zheng *et al.*, Adv. Mat. **30**, 1705318 (2018). Copyright 2018 Wiley-VCH. (b) The real part of the permittivity tensor of α-MoO_3. Three Reststrahlen bands are shaded in pink, yellow, and blue. The inset shows the unit cell of α-MoO_3, with three different oxygen sites indicated by O1–O3. (c) 3D IFCs that have biaxial hyperbolic dispersion in α-MoO_3. Reproduced with permission from Zheng *et al.*, Sci. Adv. **5**, eaav8690 (2019). Copyright 2019 Author(s), licensed under a Creative Commons Attribution-NonCommercial-NoDerivatives 4.0 International License. (d) Schematic of the scattering-type scanning near-field optical microscope with an α-MoO_3 flake. (e) Hyperbolic in-plane dispersion from the Fourier transform of the near-field images at the frequency of 893 cm^{-1}. The corresponding calculated IFC is shown by the white solid line. Reproduced with permission from Ma *et al.*, Nature **562**, 557 (2018). Copyright 2018 Springer Nature.

and out-of-plane elliptical dispersion. By exchanging the signs of ε_x and ε_y, the direction of the principal axis of the hyperbolic dispersion can be changed. The hyperbolic phonon polaritons are similar to those in uniaxial crystals such as h-BN. However, in band 3, both in-plane permittivities $\varepsilon_i (i = x, y)$ are positive and the out-of-plane permittivity ε_z is negative. In this case, both in-plane elliptical dispersion and out-of-plane hyperbolic dispersion occur. Therefore, α-MoO_3 provides a means of simultaneously controlling hyperbolic phonon polaritons in the vertical and in-plane directions. Ultra-low-loss polaritons in α-MoO_3 have been experimentally measured[63,198] with scattering-type scanning near-field optical microscopy, as shown in Fig. 9(d). The amplitude lifetime for in-plane elliptic phonon polaritons was found to be $\tau_x = 8 \pm 1$ ps, which is more than ten times longer than that of graphene plasmon polaritons at room temperature.[63,195] The amplitude lifetime for in-plane hyperbolic phonon polaritons was $\tau_x = 1.9 \pm 0.3$ ps. In the experiment, metalized, cantilevered atomic force microscope tips were used as scattering near-field probes and the infrared nanoimaging was measured by a scattering-type scanning near-field optical microscope.[63] The hyperbolic in-plane dispersion in Fig. 9(e) was obtained from the Fourier transform of the near-field amplitude image measured by the probe.[63]

III. TOPOLOGICAL TRANSITION OF DISPERSION

A. Dispersion transition from closed ellipsoids to open hyperboloids

1. Topological transition based on the frequency-dependent dispersion

Manipulating the topological properties of IFCs can provide unique control over the interaction between light and matter, such as negative refraction and increased rates of spontaneous emission. The simplest topological transition of an IFC from elliptical dispersion to hyperbolic dispersion is produced by varying the frequency in order to cause a change of the sign of the real part of the permittivity or permeability in a dispersive metamaterial. To date, most hyperbolic dispersion has been implemented by this means, in experiments including metal/dielectric multilayers, metal nanowire arrays, circuit systems, and even natural hyperbolic materials.

In metal/dielectric multilayers and metal nanowire arrays, the permittivity of the metal can be described by a Drude model,

$$\varepsilon(\omega) = \varepsilon_\infty - \omega_0^2/(\omega^2 + i\omega\gamma), \tag{18}$$

where ε_∞ is the high-frequency permittivity and ω_0 and γ denote the plasma frequency and damping frequency, respectively. At low frequency, $\varepsilon(\omega)$ is negative with a large absolute value. As the frequency increases, $\varepsilon(\omega)$ gradually tends to zero and then becomes positive. According to Eqs. (12) and (13), this allows the signs of the effective anisotropic permittivities to be tuned and the electrical topological transition of the IFC to be realized. For a circuit system with lumped elements as shown in Fig. 6(d), both the permittivity and the permeability are frequency dependent[171,172]

$$\varepsilon(\omega) = \varepsilon_a - \alpha/\omega^2, \quad \mu_\perp(\omega) = \mu_b - \beta_x/\omega^2, \quad \mu_{//}(\omega) = \mu_b - \beta_y/\omega^2, \tag{19}$$

where ε_a, μ_b, α, and $\beta_j (j = x \text{ or } y)$ are constants. Clearly, the signs of $\varepsilon(\omega)$, $\mu_\perp(\omega)$, and $\mu_{//}(\omega)$ depend on the frequency. Hence, a magnetic topological transition of the IFC can be produced by tuning the frequency.

A topological transition also can be realized in natural materials, using the dispersion of the material. Take the vdW materials as an example. The principal components of the permittivity tensor of α-MoO_3 can be described by the following Lorentz equation:[199,200]

$$\varepsilon_i(\omega) = \varepsilon_\infty^i \left(1 + \frac{{\omega_{LO}^i}^2 - {\omega_{TO}^i}^2}{{\omega_{TO}^i}^2 - \omega^2 - i\omega\Gamma^i}\right), \tag{20}$$

where ε_∞^i is the high-frequency permittivity; ω_{LO}^i and ω_{TO}^i denote the longitudinal and transversal optical phonon frequencies, respectively; and Γ^i is the damping factor. Equation (20) demonstrates that the signs of the three principal components of the permittivity tensor can be tuned by changing the frequency. As a result, a topological transition of the IFC can be implemented. Changing the frequency is, therefore, a typical means of achieving the topological transition from ellipse to hyperbola in many hyperbolic systems.

2. Loss-induced topological transition

Intrinsic loss has long been thought to be a deteriorative factor in wave propagation. For example, in a laser system, losses must be overcome by sufficient gain to reach the lasing threshold. Counterintuitively, loss-induced suppression and revival of lasing have been proposed in a non-Hermitian system with an exceptional point.[201] Loss-induced transparency[202] indicates that intrinsic loss could in fact be a beneficial parameter, revealing the need to reexamine the role of loss in electromagnetic wave manipulation. Usually, topological transitions are produced by changing the frequency. Could the topological transition instead be realized at a fixed frequency by tuning another parameter? Interestingly, that parameter can be the intrinsic loss. For metamaterials in which the real part of the permittivity or permeability vanishes, the role of loss is enhanced, even leading to a topological transition of the dispersion from a closed elliptic curve to an open hyperbolic curve. Loss can enhance transmission and produce collimation in the epsilon-near-zero (ENZ) metamaterials that have been theoretically proposed in metal–dielectric stacks[16,17] and experimentally demonstrated in a circuit-based metamaterial.[19] Using this method, wave-front manipulation and energy collimation have also been systematically studied in a metal-line system.[203] Beyond ENZ metamaterials with very flat elliptical dispersion, loss-induced topological transitions of the dispersion can occur in metamaterials that have permittivity and permeability with arbitrary positive real parts.[148] Suppose that $\mu_{//}$ is a complex number while $\mu_\perp$ is a real number. Considering the boundary conditions, the real and imaginary parts of k_z along the direction of the optical axis can be obtained from

$$k_z^2 = \mu_\perp[\varepsilon k_0^2 - (k_x^2 + k_y^2)/\mu_{//}]. \tag{21}$$

Assuming that $\varepsilon = \mu_\perp = 1$ and $\mu_{//} = 0.3 + \mathrm{Im}(\mu_{//})i$, Fig. 10(a) shows how a closed ellipsoid evolves into an open hyperboloid at a fixed frequency when the loss is changed.

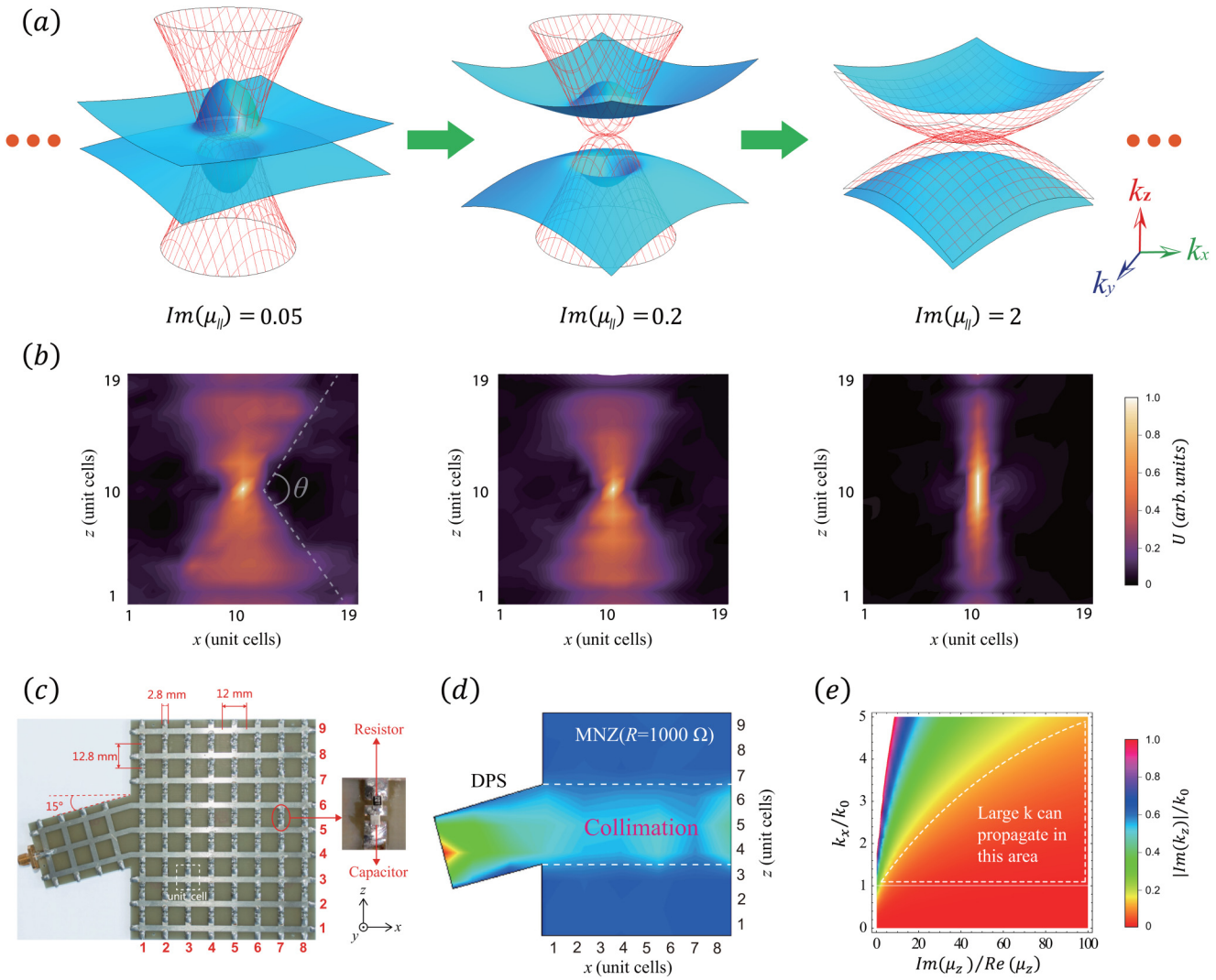

FIG. 10. (a) Topological transition of the IFC controlled by the imaginary part of $\mu_{//}$. (b) Measured emission patterns for different values of resistors at a fixed frequency. Reproduced with permission from Yu *et al.*, J. Appl. Phys. **119**, 203102 (2016). Copyright 2016 AIP Publishing LLC. (c) The circuit-based metamaterial with a wedge to demonstrate collimation. (d) The measured voltage distributions of (c) at 1.56 GHz. (e) The normalized imaginary part of k_z as a function of $\mathrm{Im}(\mu_z)/\mathrm{Re}(\mu_z)$ and k_x/k_0, when $\varepsilon = \mu_x = 1$. Reproduced with permission from Jiang *et al.*, Phys. Rev. B **91**, 045302 (2015). Copyright 2015 American Physical Society.

The cyan solid and red mesh surfaces, respectively, give the relationships of the real and imaginary parts of k_z with respect to k_x and k_y.Without loss [$\mathrm{Im}(\mu_{//}) = 0$], the IFC corresponds to a closed ellipsoid, as shown in Fig. 2(a). However, as the loss increases to $\mathrm{Im}(\mu_{//}) = 0.05$, the closed ellipsoid gradually develops a break at the center [see the left panel of Fig. 10(a)]. When the loss further increases to $\mathrm{Im}(\mu_{//}) = 0.2$, the ellipsoid is completely broken and becomes an open hyperboliclike curve [middle panel of Fig. 10(a)]. If even more loss is added, the hyperbolic curve becomes increasingly flatter and the propagation loss becomes smaller still [right panel of Fig. 10(a)]. The change in the IFC strongly modifies the propagation properties of electromagnetic waves. When the IFC becomes flat, the electric fields are collimated. The corresponding measured emission patterns of a source in a circuit metamaterial are shown in Fig. 10(b). As the loss increases, the measured emission pattern changes from two connected sectors to a column.[148] Figure 10(c) presents one sample of the circuit metamaterial, in which the loss can be flexibly controlled by resistors. By measuring the voltage pattern, loss-induced field enhancement and collimation have been observed, as in Fig. 10(d). The topological transition does not depend on the real part of $\mu_{//}$, as shown in Fig. 10(e); for an arbitrary real part of $\mu_{//}$, the topological transition will occur provided

the imaginary part of $\mu_{//}$ is large enough. Therefore, without using gain to compensate the loss,[204,205] tuning the anisotropic loss is an effective way to control the dispersion.

3. Actively controlled topological transition

A topological transition of the dispersion in passive systems can be created by changing the frequency or adding anisotropic loss. However, the ability to actively tune these effects remains elusive and related experimental observations are highly desirable. Tuning the topology of the IFC in an active manner has become a very interesting topic of late because of its usefulness in the design of new active devices. Recently, a novel implementation of the topological transition based on 2D semiconductors, such as graphene, was proposed. Varying the chemical potential of graphene using the gate voltage is an effective method to control the conductivity of graphene in the terahertz and infrared frequency regimes.[206–208] The combination of metamaterials and graphene provides options for actively manipulating electromagnetic waves, such as graphene-based metasurfaces,[209,210] subwavelength focusing,[211] negative refraction,[212] and slow light.[213] A schematic of a graphene/dielectric multilayer structure is shown in Fig. 11(a). The dielectric layers are marked in cyan, and the graphene layers are shown by the single layer of carbon atoms.

The effective permittivity of a graphene sheet is characterized by its surface conductivity $\sigma(\omega, \mu_c)$ as[206]

$$\varepsilon_g = 1 + i\sigma(\omega, \mu_c)/\varepsilon_0\omega t_g, \tag{22}$$

where μ_c and t_g denote the chemical potential and the thickness of the graphene sheet. σ is a complex number with a large imaginary part, so ε_g can become negative in certain frequency ranges. Specifically, μ_c can be tuned by varying the gate voltage. The permittivity of the graphene sheet can, therefore, be tuned by changing the value of μ_c. In certain frequency regimes, ε_g takes a large negative value and the graphene sheet displays metallic properties.

The permittivity and thickness of the dielectric layer are 2.25 and 50 nm, respectively.[212] From Eq. (12), the anisotropic permittivity tensor of the graphene/dielectric multilayer structure can be obtained. Both the value and the sign of $\varepsilon_{//}$ can be flexibly adjusted by changing the value of μ_c. As the value of μ_c increases from 0.1 to 1 eV, the sign of $\varepsilon_{//}$ reverses at 0.54 eV while the sign of $\varepsilon_{\perp}$ remains positive, as shown in Fig. 11(b). The hyperbolic regime and the elliptical regime are marked in Fig. 11(b). In addition, using an array of graphene strips, researchers actively tuned the dispersion from an elliptic curve to a hyperboliclike curve by changing the external gate voltage.[86,87] The corresponding dispersion relation equation is written as[86]

$$\eta_0^2(k_x^2\sigma_{xx} + k_y^2\sigma_{yy})^2(k_x^2 + k_y^2 - k_o^2) - 4k_o^2(k_x^2 + k_y^2)^2 = 0, \tag{23}$$

where η_0 denotes the impedance of the free space. The effective conductivity tensor in an HMS consisting of a graphene strip array is presented in Fig. 11(c). When the condition $\mathrm{Im}(\sigma_{xx})\,\mathrm{Im}(\sigma_{yy}) < 0$ is satisfied, hyperbolic dispersion is obtained. The topological transition from a closed ellipse to an open hyperbolic dispersion is associated with the change from $\mathrm{Im}(\sigma_{xx}) < 0$, $\mathrm{Im}(\sigma_{yy}) < 0$ to $\mathrm{Im}(\sigma_{xx})\,\mathrm{Im}(\sigma_{yy}) < 0$. The propagation direction of SPPs in the graphene HMS is controlled by varying the value of μ_c. Figures 11(d) and 11(e) display the distributions of the electric field magnitude when SPPs are excited for $\mu_c = 0.1$ and 0.3 eV, respectively.

In the high-frequency region, fabricating the multilayers becomes more difficult and it is not easy to apply precisely the same external voltage to each graphene layer.[214–216] However, in the microwave regime, circuits loaded with variable capacitance diodes provide a flexible platform to experimentally demonstrate an actively controlled topological transition. In these circuits, the value of the capacitance can be actively tuned by an external voltage. The inverse or zero Doppler effect and frequency mixing have been observed in 1D circuit systems.[217–219] A topological phase transition has been achieved in a 2D circuit sample, shown in Fig. 11(f). A direct voltage source is connected to the sample from the top, marked by the red arrow. The signal is input at the center of the sample.[149] According to Eq. (17), the anisotropic permeability of the circuit-based metamaterial can be tuned by changing the capacitance. As the voltage increases, the capacitance of the varactor decreases accordingly. Therefore, a topological transition from elliptic dispersion to hyperbolic dispersion occurs. For example, when U = 1 V, the IFC is a closed elliptical curve and the radiation emitted by the source can propagate in all in-plane directions, as shown in Fig. 11(g). However, when U = 20 V, the IFC becomes an open hyperbolic curve and the source can only radiate in certain directions, as shown in Fig. 11(h). Active control of the topological transition of the dispersion by changing the external voltage can, therefore, be easily observed in circuit-based metamaterials.

B. Transition points in two types of topological transitions

1. Anisotropic zero-index metamaterials

By changing the sign of $\mu_{//}$ from a positive value to a negative value while the sign of ε and $\mu_{\perp}$ remain positive, a topological transition will occur, as illustrated in Fig. 12(a). Near the point where $\mu_{//}$ changes from a positive value to 0, the IFC changes from an ellipsoid to a very flat ellipsoid. When $\mu_{//}$ becomes negative, the IFC changes to an open hyperboloid. At the transition point ($\mu_{//} \to 0$), the material becomes an anisotropic mu-near-zero (AMNZ) material whose IFC is a very flat ellipsoid. Although this discussion is based on a magnetic-type hyperbolic topological transition, a similar argument can be extended to the electric-type hyperbolic topological transition when the permittivity and permeability are exchanged. At the transition point of the electric-type topological transition, the material becomes an anisotropic epsilon-near-zero (AENZ) material. Many unusual transport properties of light in AENZ and AMNZ metamaterials have been demonstrated, such as spatial power combination,[220] bending waveguides,[221–223] field shielding,[224] total reflection,[225] and perfect absorption.[226] Interestingly, it has been found that flux manipulation can be achieved in anisotropic zero-index metamaterials.[227–230] When scatterers are placed in the background material, the inhomogeneity profile $f(x, z)$ is a spatially varying function. For ordinary background material (such as air), incident light will be scattered by different scattering objects. As the scattered waves distribute energy flux in all directions, transmission in the forward direction is reduced. However, the scattering phenomenon is

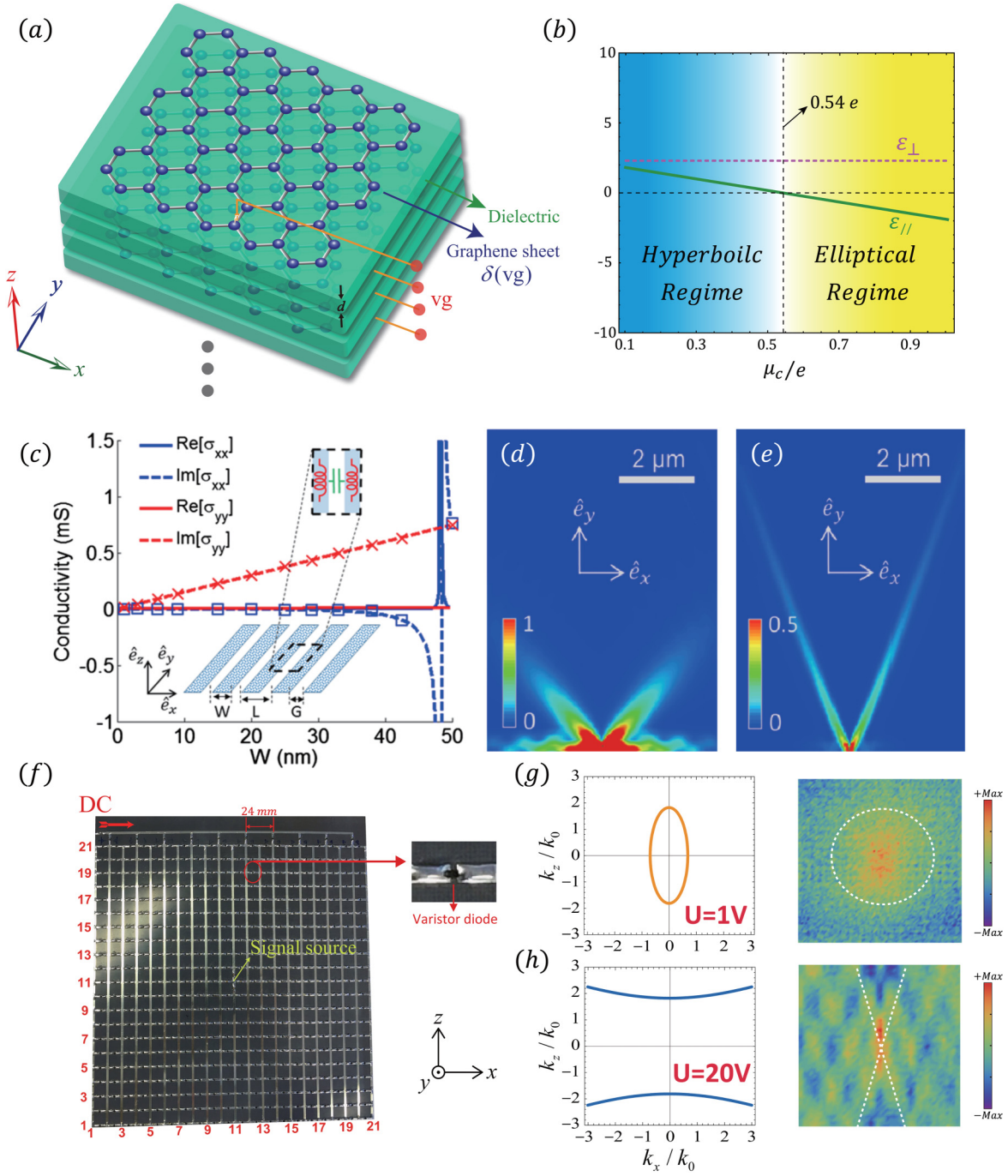

FIG. 11. (a) Schematic of the graphene–dielectric multilayers. The chemical potential of the graphene layer can be tuned with the external voltage, and for certain external voltages, this multilayer structure has hyperbolic dispersion. (b) Real parts of $\varepsilon_{\perp}$ and $\varepsilon_{//}$ for the multilayer structure at a fixed frequency of 40 THz. (c) Effective conductivity tensor of a uniaxial HMS consisting of graphene strips. (d) Distribution of the electric field for SPPs excited on the graphene HMS for $\mu_c = 0.1$ eV. (e) As (d), but for a chemical potential of 0.3 eV. Reproduced with permission from Gomez-Diaz *et al.*, Phys. Rev. Lett. **114**, 233901 (2015). Copyright 2015 American Physical Society. (f) Circuit-based metamaterials that can be actively tuned by an externally applied voltage. The inset shows an enlarged view of the lumped varactor diode. (g) The IFC and the measured electric field E_y for U = 1 V. (h) As (g), but for U = 20 V. Reproduced with permission from Guo *et al.*, Appl. Sci. **8**, 596 (2018). Copyright 2018 Author(s), licensed under a Creative Commons Attribution-NonCommercial-NoDerivatives 4.0 International License.

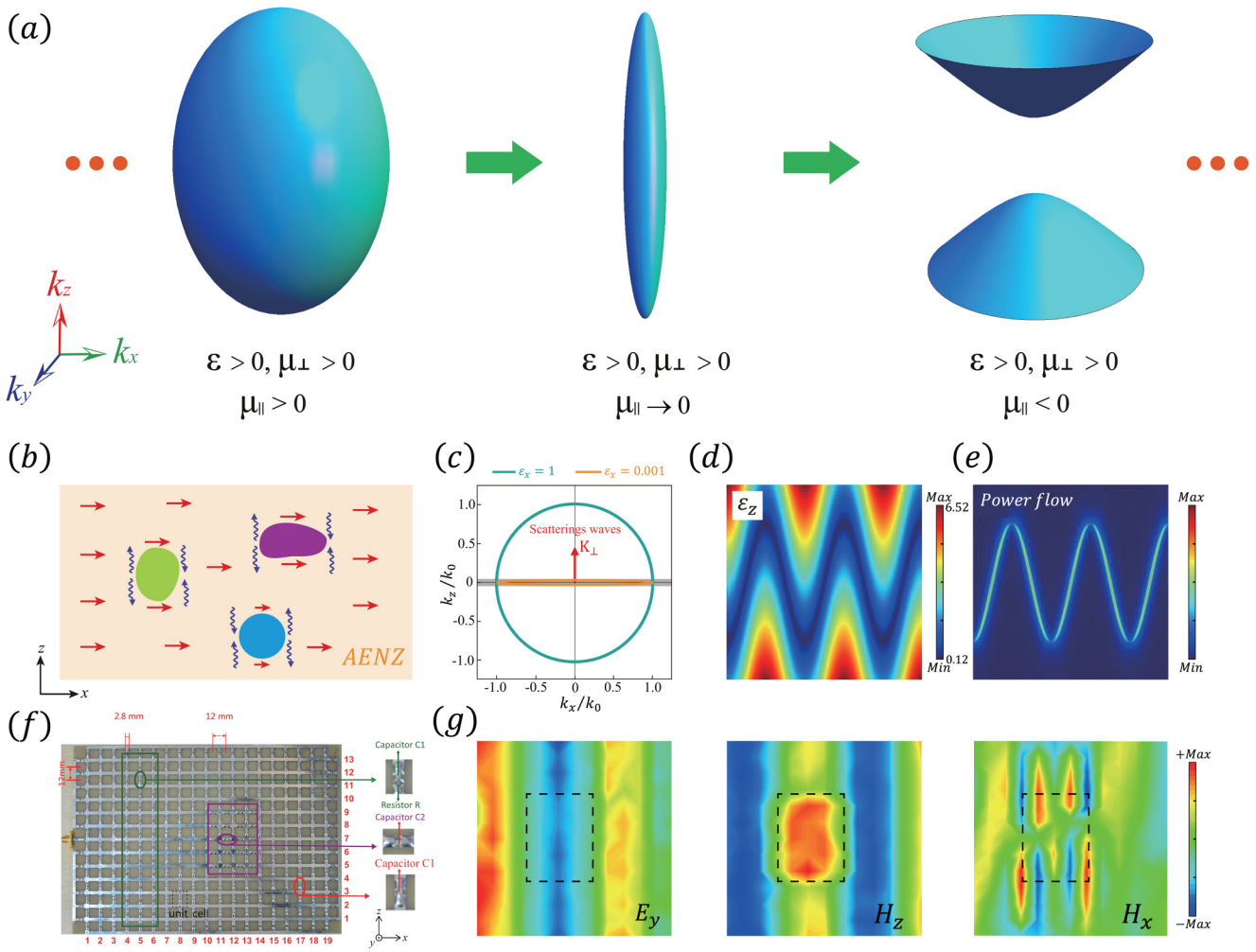

FIG. 12. (a) Magnetic topological transition of the IFC from a closed ellipsoid to an open hyperboloid when $\mu_{//}$ changes from a positive value to a negative value, while ε and $\mu_\perp$ remain unchanged. (b) Schematic of electromagnetic wave propagation and scattering in an AENZ system with defects. (c) IFCs of air and the AENZ background medium. $K_\perp$ denotes the perpendicular component of the wave-vectors of the scattered waves. (d) The spatial inhomogeneity profile that has a sinusoidal pathway of minimal ε_z. (e) The corresponding distribution of power flow. Reproduced with permission from Luo *et al.*, Phys. Rev. Lett. **112**, 073903 (2014). Copyright 2014 American Physical Society. (f) Circuit-based AMNZ metamaterial, with a defect region marked by the purple rectangle. (g) Measured field distributions of E_y, H_z, and H_x from columns 7–19 in the sample shown in (f). Reproduced with permission from Li *et al.*, Europhys. Lett. **113**, 57006 (2016). Copyright 2016 Institute of Physics.

strongly modified in an AENZ metamaterial ($\varepsilon_x \to 0^+$), as in Fig. 12(b). In this case, the scattered waves become evanescent waves in the horizontal direction instead of propagating waves in all directions. The physical mechanism can be understood from the IFC in Fig. 12(c). The cyan circle and orange ellipse correspond to the IFCs of air and the AENZ medium, respectively. After the wave is scattered by a defect, a series of waves with perpendicular wave-vectors in the z direction ($K_\perp$) are excited. When the scattering occurs in a background material of air, $K_\perp$ still falls within the maximum value of the IFC of air in Fig. 12(c), and the scattered wave is still a propagating wave in various directions. However, for scattering that occurs in the AENZ metamaterial, $K_\perp$ falls outside the maximum values of k_z of the IFC [orange flat ellipse in Fig. 12(c)]. Due to the mismatch of the tangential wave-vectors ($K_\perp$ and k_z of the IFC), evanescent waves are excited. This difference in scattering behavior produces completely different scattering propagation phenomena, which enable entirely new ways of regulating electromagnetic energy flow at the subwavelength scale. Owing to the excitation of evanescent scattered waves in this inhomogeneous and AENZ metamaterial, the electromagnetic energy flux can be controlled according to the spatial profile of the nonzero ε or μ component. Electromagnetic flux control in the AENZ metamaterial can be readily demonstrated when the spatial inhomogeneity profile has a sinusoidal pathway of minimal ε_z, as

shown in Fig. 12(d). The simulated power flow distribution in Fig. 12(e) shows that the energy flux flows along the designated sinusoidal path. This energy flow manipulation has been experimentally demonstrated in an AMNZ metamaterial, as seen in Fig. 12(f). The sample was constructed using a circuit system with lumped elements. The measured field distributions are shown in Fig. 12(g), where E_y is uniform in the z direction. However, compared with the background medium, H_z in the scattering region is enhanced and H_x is excited as an evanescent wave. Figure 12(g) shows that magnetic components can be controlled at the subwavelength scale in an AMNZ metamaterial.

2. Linear-crossing metamaterials

From Eq. (6), it is evident that the IFC of magnetic HMMs is not only related to the anisotropic permeability but also to the permittivity. Normally, a topological transition between two types of magnetic hyperbolic metamaterials will take place when the signs of the anisotropic permeabilities are exchanged and the permittivity is held fixed. However, a new type of linear-crossing dispersion exists when the sign of the permittivity changes while the signs of the anisotropic permeabilities remain unchanged, as shown in Fig. 13(a). In the 2D case, when $\mu_{\perp}\mu_{//} < 0$ and $\varepsilon \to 0$, the IFC at the transition point between a metal-type HMM and a dielectric-type HMM takes the form of two intersecting lines. This material with two intersecting linear dispersion curves can be termed a linear-crossing metamaterial (LCMM). Because the signs of the in-plane permeabilities are opposite and the permittivity tends to zero, an LCMM may simultaneously possess the characteristics of an HMM and a zero-index medium. On the one hand, similarly to an HMM, high-k waves can be supported by the LCMM because of the open IFC. In addition, positive and negative refraction can be controlled by the signs of the in-plane permeabilities as in an HMM. The 2D IFC of an LCMM with negative refraction is shown in Fig. 13(b). On the other hand, the group velocity and phase velocity in an LCMM are perpendicular to each other, which lead to zero phase accumulation along the propagation path as in a zero-index medium. LCMMs possess many unique properties.[22] For example, directional propagation can be observed when light is obliquely incident on the LCMM, as shown in Fig. 13(c). Unlike negative refraction in a double negative metamaterial, the refraction angle in an LCMM is independent of the incidence angle. A novel beam splitting phenomenon[231,232] occurs in an LCMM when light is normally incident on the structure, as shown in Fig. 13(d).[22] Owing to the fact that the refracted light is locked in two fixed directions in the LCMM, the propagation of light is not affected by the inner defect as long as the defect is not placed in the path of refraction. In circuit systems, two types of LCMMs with positive and negative refraction, respectively, have been constructed. Due to the negative refraction, imaging of a point source can be carried out. Moreover, since the propagation of waves in LCMMs is fixed in two directions, the imaging exhibits a partial cloaking effect.[22] For two sources separated by a subwavelength distance, super-resolution with a partial cloaking effect may be realized. The super-resolution mechanism results from the open IFC of LCMMs, which will support high-k modes. Therefore, LCMMs can be used to overcome the diffraction limit.[22] Super-resolution imaging with partial cloaking has been experimentally demonstrated, as shown in Fig. 13(e). The measured distribution of the normalized electric field is plotted in Fig. 13(f). The reflections from the sidewalls are weak because all of the structure boundaries are absorption boundaries. The defect region is marked by the dashed yellow rectangle, and the positions of images are marked by the two dashed red circles. In order to quantitatively demonstrate subwavelength imaging with a partial cloaking effect, the normalized intensity of the electric fields at the exit plane in two cases, with and without defects, is shown in Fig. 13(g). Recently, an omnidirectional invisibility cloak for a wide range of incident angles has also been discovered in an anisotropically doped ENZ metamaterial, which is transparent to any incident illumination.[233]

IV. DISPERSION CONTROL IN HYPERCRYSTALS

A. Controlling dispersion of the band structure

Because of the unusual properties of HMMs, composite structures involving HMMs may also be expected to exhibit unprecedented abilities to manipulate electromagnetic waves. Recently, Narimanov studied a structure in which one dielectric component of a one-dimensional (1D) photonic crystal (PC) was replaced by a HMM component, named a photonic hypercrystal (PHC).[97] In a PHC, the special dispersion of the HMM strongly modifies the Bragg scattering and thereby allows the bandgaps of the structure to be manipulated, as we will see later.

The most remarkable feature of PCs is that they have photonic bandgaps, which can be used to suppress spontaneous emission[234] and localize photons.[235] In particular, an omnidirectional gap based on 1D PCs is very useful in many applications, such as optical reflectors for all angles of incidence.[236] In traditional dielectric PCs $(AB)_n$, the bandgaps arise from the Bragg scattering mechanism. At the Bragg frequency of the first bandgap, the Bragg condition is written as

$$\phi = (k_{Az}d_{Az} + k_{Bz}d_{Bz})|_{\omega Brg} = m\pi, \tag{24}$$

where k_{Az} and k_{Bz} are the wave-vectors in the propagation direction in medium A and B, respectively. ϕ denotes the propagation phase in a unit cell. The dispersion relation for a dielectric is $k_x + k_z = \varepsilon\mu(\omega/c)^2$, where $k_x = k_0 \sin\theta$ is the parallel wave-vector. When the incidence angle θ increases, k_x increases while k_{Az} and k_{Bz} decrease. If the frequency remains at ω_{Brg}, the Bragg condition in Eq. (24) no longer holds. As a result, to maintain the Bragg condition, the frequency must increase. Therefore, as the incidence angle increases, the gap will shift toward a higher frequency. In a traditional 1D PC, the gap edges change with the incidence angles and the gap closes at the Brewster angle. To overcome this problem, omnidirectional gaps independent of the incidence angles have been proposed in special 1D PCs, including the average index (zero-$\bar{n}$) gap that exploits the mechanism of phase cancellation of propagating waves between positive- and negative-index materials[237–241] and the zero effective phase (zero-ϕ_{eff}) gap that utilizes compensation between the exponentially increasing and decreasing waves in two types of single-negative materials.[242–245]

The PHC provides a new physical mechanism for designing angle-independent (dispersionless) gaps. The schematic of a 1D

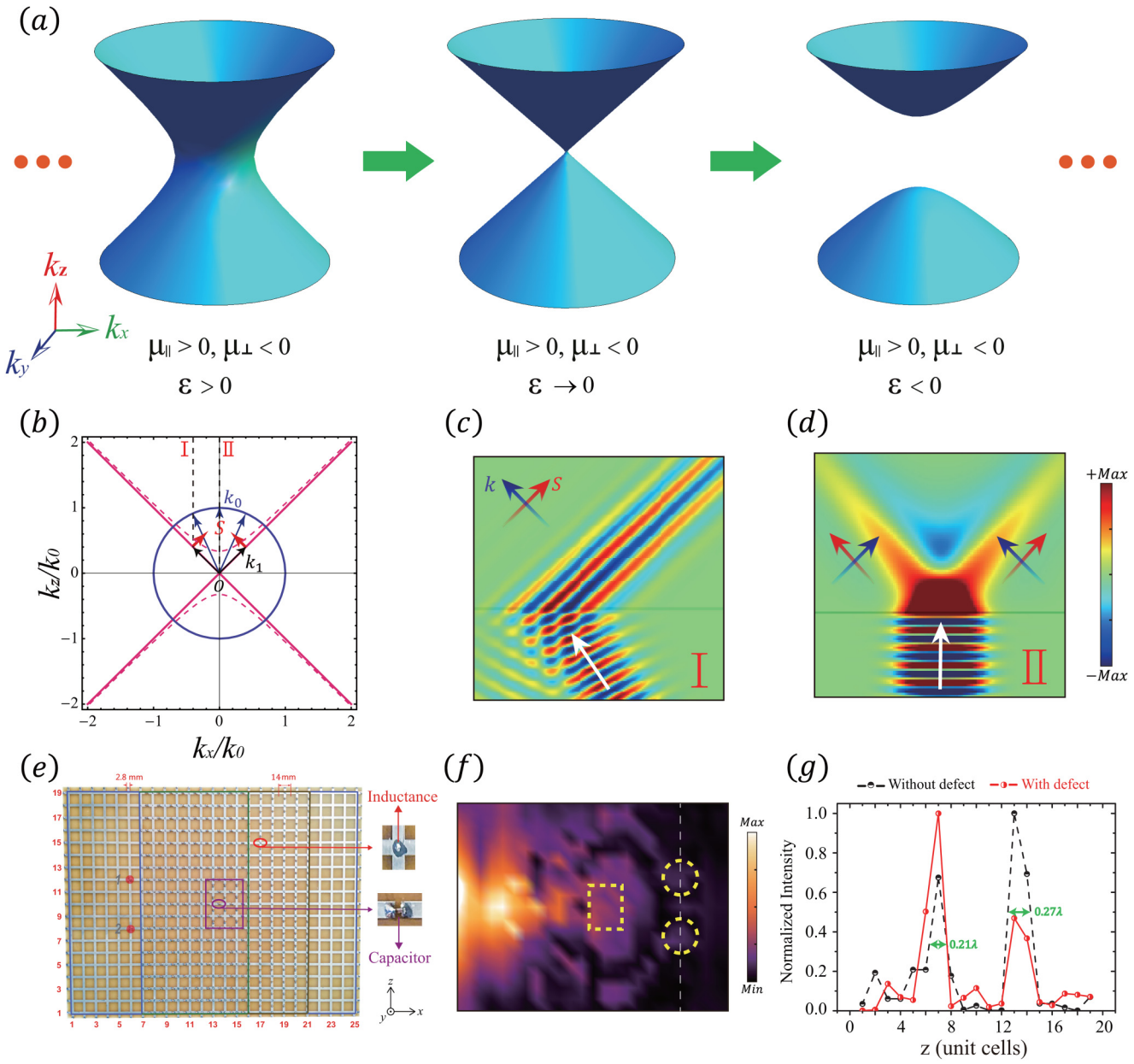

FIG. 13. (a) Magnetic hyperbolic topological transition of the IFC from metal-type hyperbolic dispersion to dielectric-type hyperbolic dispersion when ε changes from a positive value to a negative value, while $\mu_{//}$ and $\mu_{\perp}$ remain unchanged. (b) The IFC of an LCMM with $\mu_z = 1$, $\mu_x = -1$, and $\varepsilon \to 0$. (c) Negative refraction independent of the incident angle takes place in the LCMM at oblique incidence. (d) The normally incident light splits along two directions in the LCMM. (e) Circuit-based LCMMs. Two sources are marked by red dots. (f) Measured distribution of the normalized electric field. Two images are marked by yellow circles. (g) Normalized field intensity distributions along the *z* direction at the exit plane. Reproduced with permission from Guo *et al.*, Phys. Rev. Appl. **10**, 064048 (2018). Copyright 2018 American Physical Society.

PHC is shown in Fig. 14(a). Suppose that layer *A* is an HMM while layer *B* is dielectric. Figure 14(b) demonstrates that the slopes of the isofrequency curves of the dielectric and the HMM have opposite signs. When the incidence angle increases, k_x increases. The isofrequency curve indicates that when k_x increases, k_{Bz} or the phase in layer *B* decreases, but k_{Az} or the phase in layer *A* increases. Therefore, as the incidence angle increases, the phase variations in the two media have opposite signs. It is this phase variation compensation (PVC) effect that leads to the dispersionless gap. Note that it is phase *variation* compensation rather than phase

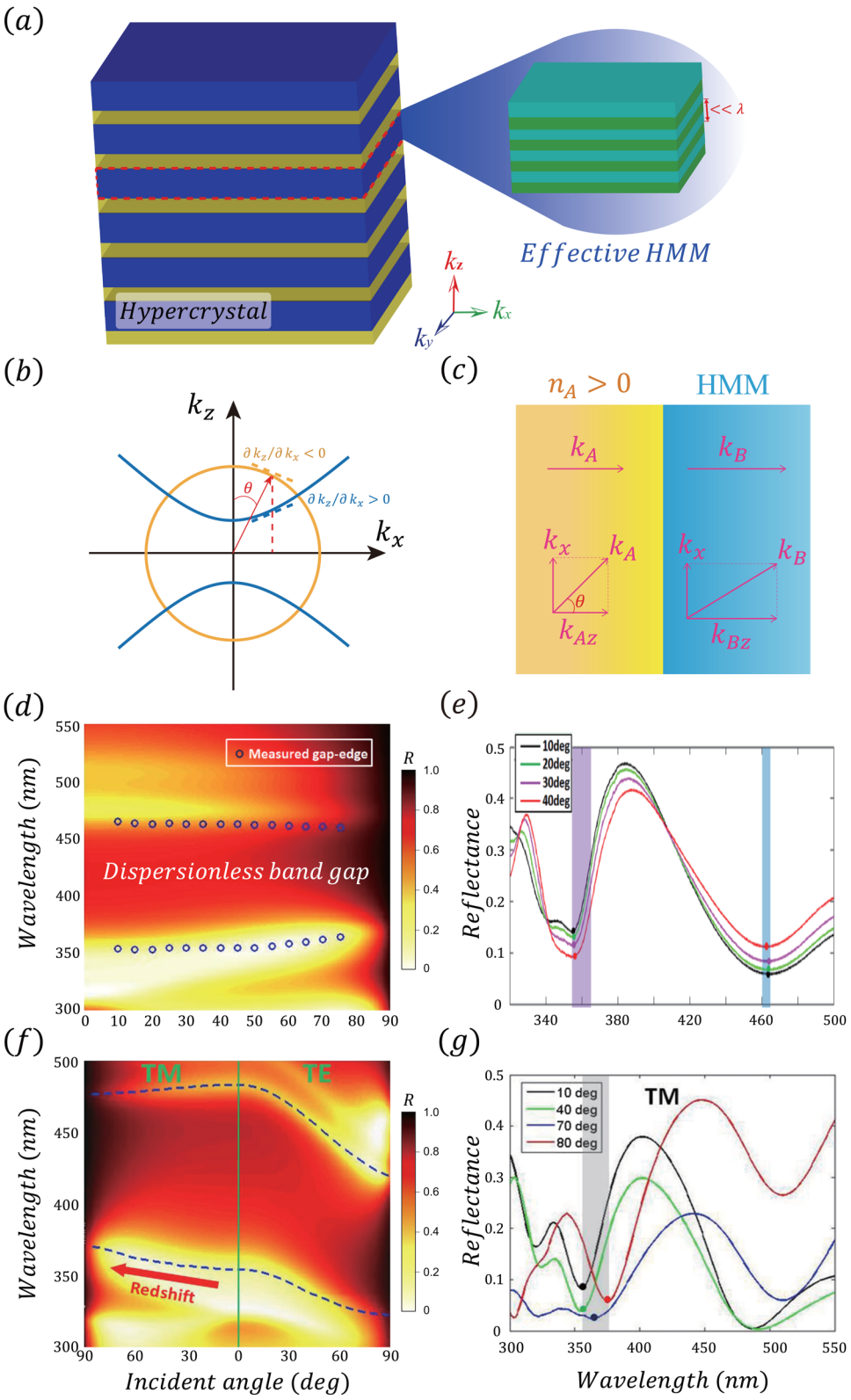

FIG. 14. (a) Schematic of a 1D PHC composed of an HMM layer and a dielectric layer. The enlargement demonstrates that the HMM layer may be mimicked by a metal/dielectric layered structure. (b) IFCs of the HMM and the dielectric medium in (a), shown as blue and orange lines, respectively. (c) Schematic of a plane wave propagating in one unit cell of the 1D PHC. (d) The reflection spectrum of the 1D PHC ($[TiO_2/HMM]_3$) for TM waves. The HMM consists of two subwavelength unit cells ($[TiO_2/Ag]_2$). (e) Measured reflectance at incidence angles of 10°, 20°, 30°, and 40°. Reproduced with permission from Wu *et al.*, Appl. Phys. Lett. **112**, 041902 (2018). Copyright 2018 AIP Publishing LLC. (f) Similar to (d), but for two types of polarization; the thicknesses of the metal and dielectric layers are adjusted slightly. (g) Measured reflectance at incidence angles of 10°, 40°, 70°, and 80°. Reproduced with permission from Wu *et al.*, Phys. Rev. Appl. **10**, 064022 (2018). Copyright 2018 American Physical Society.

compensation because the total phase is still π. From Eq. (24), the condition for the dispersionless gap is[246]

$$\frac{\partial \Phi}{\partial k_x} = \left(d_A \frac{\partial k_{Az}}{\partial k_x} + d_B \frac{\partial k_{Bz}}{\partial k_x} \right)\Big|_{\omega_{\mathrm{Brg}}} = 0. \tag{25}$$

The PVC condition for the dispersionless gap can be analytically approximated in the $\varepsilon_B \gg 1$ and $|\varepsilon_{Az}| \gg 1$ limit as[246]

$$d_A = \frac{\pi c}{\omega_{\mathrm{Brg}}} \frac{1}{\sqrt{\varepsilon_{Ax}}\left(1 - \frac{\varepsilon_B}{\varepsilon_{Az}}\right)}, \quad d_B = \frac{\pi c}{\omega_{\mathrm{Brg}}} \frac{1}{\sqrt{\varepsilon_B}\left(1 - \frac{\varepsilon_{Az}}{\varepsilon_B}\right)}. \tag{26}$$

The phase compensation effect can be explained as in Fig. 14(c). Based on the PVC condition, the calculated reflection spectrum of a 1D PHC ($[TiO_2/HMM]_3$) for TM waves is given in Fig. 14(d). The HMM is realized by two subwavelength unit cells ($[TiO_2/Ag]_2$). The measured reflectance spectra at the corresponding incidence angles are shown in Fig. 14(e). The two band edges (reflective dips near the bandgap) change very little as the incidence angle changes from 10° to 40°. The measured gap edges are marked in Fig. 14(d); the experimental results coincide well with the simulated results.[247] In addition to the dispersionless bandgap, a red shift of the bandgap can be realized according to the condition $\partial\Phi/\partial k_x > 0$, which is distinct from the blue shift of the bandgap that occurs in conventional dielectric PCs. The simulated and measured results of red shifted bandgaps for TM waves are shown in Figs. 14(f) and 14(g), respectively.[248] It should be pointed out that, for TE ordinary waves, the subwavelength metal/dielectric multilayer structure behaves just like a dielectric. As a result, the bandgap is blue shifted, as shown in Fig. 14(f).

B. Cavity modes and edge modes with special dispersion

Dispersionless gaps can be used to realize wide-angle cavity modes. The quality factor of the dispersionless cavity mode remains essentially unchanged when the plane waves launch at different angles, which is valuable when the cavity mode is excited with finite-size sources. A schematic of a 1D PHC with a dielectric defect marked in pink is shown in Fig. 15(a). It is seen in Fig. 15(b) that the defect or cavity mode inside the dispersionless gap remains nearly invariant as the incidence angle changes, owing to the PVC effect.[246]

Moreover, in a heterostructure composed of a 1D PC and a metal [Fig. 15(c)], an edge mode occurs at the interface of the 1D PC and the metal.[249] The phase matching condition for edge states can be expressed as[250–252]

$$\phi_M + \phi_{pc} = 0, \quad \phi_M, \phi_{PC} \in (-\pi, \pi), \tag{27}$$

where ϕ_M and ϕ_{pc} denote the reflection phases of the metal layer and the 1D PC, respectively. Owing to this condition for the edge

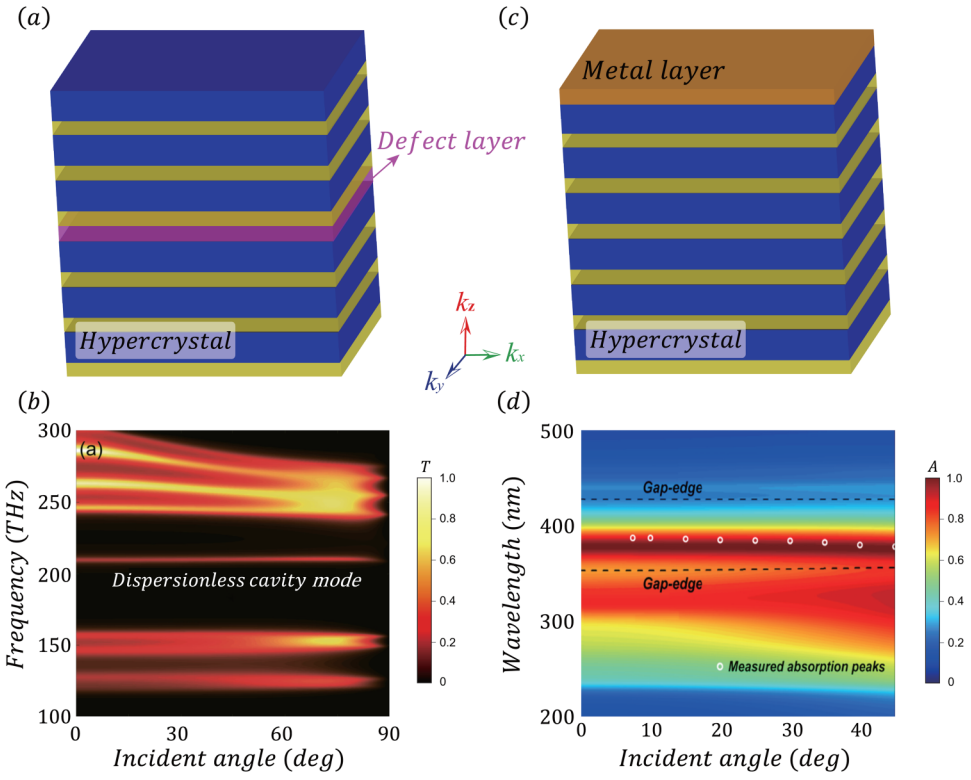

FIG. 15. (a) Schematic of a 1D PHC with a defect layer at the center of the structure. (b) Transmittance spectrum of (a) for all angles of incidence. Reproduced with permission from Xue *et al.*, Phys. Rev. B **93**, 125310 (2016). Copyright 2016 American Physical Society. (c) Schematic of a heterostructure composed of a metal layer and a 1D PHC. (d) Absorption spectrum of (c) from 0° to 45°. Some measured absorption peaks are marked by white hollow circles. Reproduced with permission from Lu *et al.*, Opt. Express **27**, 5326 (2019). Copyright 2019 OSA Publishing.

mode, the reflection phase of the metal changes very little with the incidence angle. This means that the dispersion properties of the edge mode are essentially determined by the 1D PC. A nearly dispersionless edge mode can be obtained in a heterostructure composed of a metal layer and 1D PHC because of the dispersionless gap of the 1D PHC. In this nearly dispersionless edge mode, light can enter the heterostructure and be fully absorbed by the lossy metal. The measured absorption peaks, marked by white circles, and the simulated absorption spectrum are shown in Fig. 15(d).[253] The experimental results agree well with the simulated results. The absorption peak is always near one over a wide range of incidence angles. Therefore, using dispersionless gaps, wide-angle perfect absorbers can be designed.[249]

Recently, the dispersion control possible in PHCs has been employed in proposals to produce Dirac dispersion,[254] to design wide-angle biosensors,[255] and to construct a Veselago lens.[256] In addition to the 1D PHCs, 2D PHCs have also been proposed. These can greatly enhance the light-matter interaction, with applications that include increasing the spontaneous emission[257–259] and designing accidentally degenerate double Dirac cones.[260,261]

V. APPLICATIONS

A. Hyperlens

In imaging optics, information regarding objects is carried by the scattered field with various wave-vectors. In particular, large features (fine details) are carried by the propagating waves (evanescent waves) with small (large) wave-vectors. For a conventional lens, the evanescent waves are confined to the near-field region and decay exponentially with transmission distance, as shown in the upper row of Fig. 16(a). The missing subwavelength information leads to the diffraction limit of imaging. By using evanescent field amplification, the diffraction limit can be overcome and imaging quality can be greatly improved.[128,262,263] Owing to the coupling of the interface modes, the near-field components can be recovered at the image plane. According to this physical principle, a silver film with $\varepsilon = -1$ has been used to achieve subwavelength imaging, verifying the potential for superlens applications.[262]

In addition to the superlens based on near-field amplification, a hyperlens based on the conversion of near fields into far fields can also yield subdiffraction-limited resolution.[45,46] One of the most fascinating features of HMMs is that they support large-k modes because of the open hyperboloid dispersion. HMMs can convert near fields into high-k propagating waves and thus overcome the diffraction limit, as shown in the lower row of Fig. 16(a). A cylindrical prototype of a hyperlens was obtained by bending flat layers (metal/dielectric multilayers) into curved layers, as shown in Fig. 16(b). The resolution and magnification of the hollow cylinder hyperlens can be estimated from the ratio between the inner and outer radii of the structure. A hyperlens beyond the diffraction limit has also been proposed for photolithography. It can be used to generate deep subwavelength patterns from diffraction-limited masks, as illustrated in Fig. 16(c).[264,265] Another type of hyperlens may be realized with a nanometal wire array at near-infrared and midinfrared wavelengths,[266,267] producing a quarter-wave image that can be clearly observed in the image plane. Although hyperlenses with open hyperbolic dispersion are excellent for producing super-resolution imaging, elliptical dispersion (as in anisotropic zero-index metamaterials) can also be used for superlenses as long as the coverage of lateral wave-vectors is sufficiently large.[268]

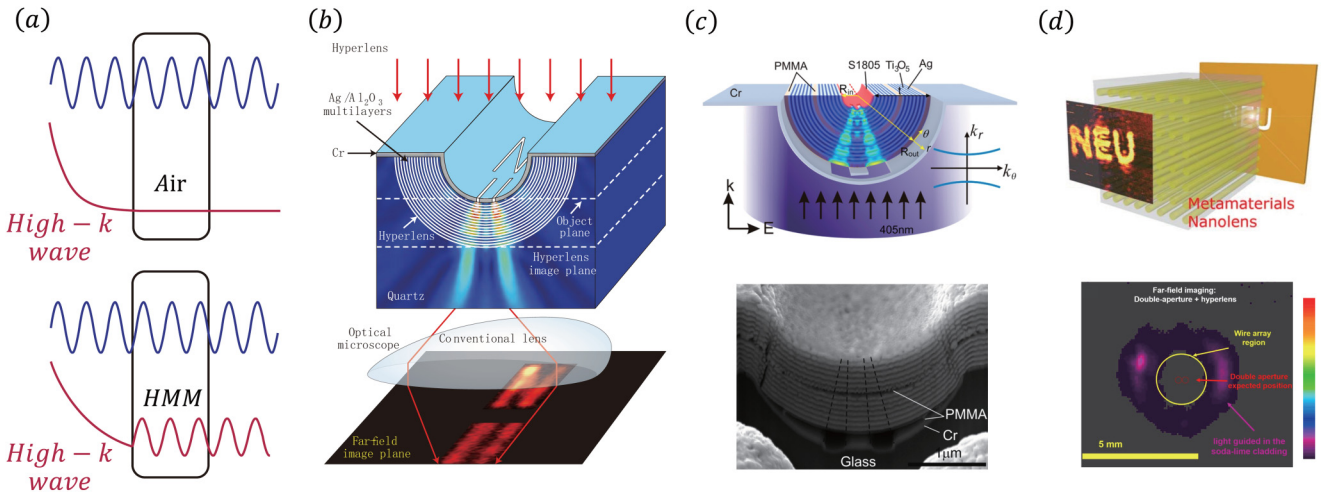

FIG. 16. (a) Schematics of a conventional lens and a hyperlens. Reproduced with permission from Zhang and Liu, Nat. Mater. **7**, 435 (2008). Copyright 2008 Springer Nature. (b) Hemicylindrical hyperlens composed of metal–dielectric multilayers. Reproduced with permission from Liu *et al.*, Science **315**, 1686 (2007). Copyright 2007 American Association for the Advancement of Science. (c) Light photolithography with a hyperlens. Reproduced with permission from Sun and Litchinitster, ACS Nano **12**, 542 (2018). Copyright 2018 American Chemical Society. (d) Hyperlens comprised of a nanometal wire array and its far-field images. Reproduced with permission from Casse *et al.*, Appl. Phys. Lett. **96**, 023114 (2010). Copyright 2010 AIP Publishing LLC and Hayashi *et al.*, Opt. Express **27**, 21420 (2019). Copyright 2019 OSA Publishing.

B. Long-range energy transfer

The interaction between two dipoles is a basic physical effect that plays an important role in many phenomena, such as the Casimir force, van der Waals force, and vacuum friction.[269,270] The interaction between two dipoles is based on the near-field coupling mechanism. A near field with a large wave-vector component decays rapidly as the spatial distance increases. Therefore, within the environment of a vacuum or an ordinary medium, the interaction distance between two dipoles is very short, generally much smaller than one wavelength. However, the emergence of HMMs suggests the possibility of overcoming the limitation of the short-range interaction in traditional environments. HMMs can support large wave-vector modes. Hence, in HMMs, the near field can be converted into high-k propagating waves, as shown in Fig. 17(a). Recent theoretical studies have shown that the interaction distance between two dipoles can be greatly increased, up to the order of one wavelength, by using HMMs.[52–55] Figure 17(b) shows that two dipoles placed on an HMS can experience long-range interaction.[53] θ_{xy} denotes the angle with respect to the optical axis of the HMS. The cooperative Lamb shift along the resonance cone angle $\theta_{xy} = \tan^{-1}\sqrt{-\varepsilon_{\perp}/\varepsilon_{//}}$ is shown in Fig. 17(c) as a function of the separation distance. The inset in Fig. 17(c) shows giant enhancement of Förster resonance energy transfer.[53]

HMMs can also be utilized to greatly enlarge the coupling distance between a dipolelike bright atom and a quadrupolelike dark atom.[56] Similar to the three-level atomic system, the classical analog of electromagnetically induced transparency (EIT) in metamaterial systems requires significant coupling between the bright atom and dark atom modes.[271–273] In a conventional medium, the separation distance for near-field coupling between the bright and dark atoms needs to be ∼λ/20–λ/40, where λ is the operational wavelength. However, in an HMM, long-range EIT in which the bright and dark atoms are separated by a long distance has been observed in a microwave experiment. The microwave HMM was constructed based on a circuit system with lumped elements, as shown in Fig. 17(d). Compared to ordinary materials, the coupling length can be increased by nearly two orders of magnitude in the HMM. Accordingly, the energy transfer from the bright atom to the dark atom can be greatly enhanced. The long-range energy transfer is shown in Fig. 17(e). The HMM-mediated EIT survives even when the coupling distance is far beyond the effective near-field coupling length in a normal environment, as shown in Fig. 17(f).

C. High-sensitivity sensors

HMMs can be utilized to create various highly sensitive sensors, such as refractive index sensors, by exciting the high-k modes.[274–280] The high-k modes in HMMs respond to changes in the refractive index and have high sensitivity in biosensing applications. Two important HMM-based sensors in the visible and near-infrared ranges have been demonstrated, based on metal/dielectric

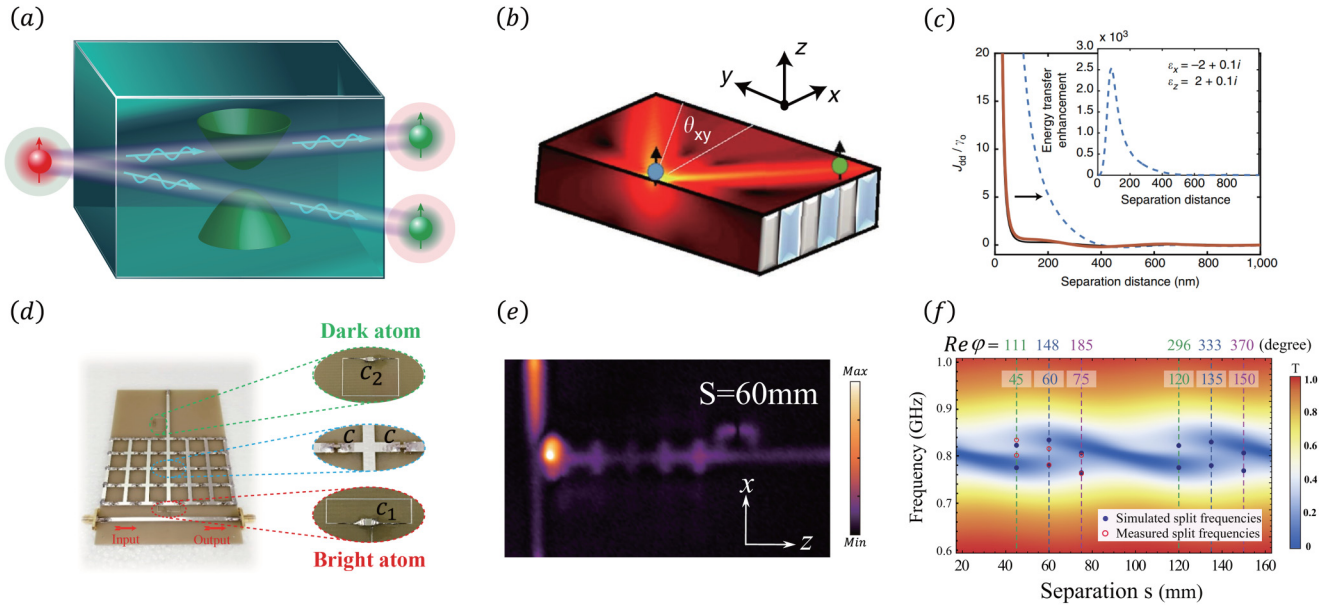

FIG. 17. (a) Schematic of HMM-assisted energy transfer between bright and dark atoms. (b) Long-range dipole–dipole interaction produced by the HMS. The blue dot and green dot denote the emitting dipole and receiving dipole, respectively. (c) Cooperative Lamb shift as a function of the separation distance along the resonance cone angle. Reproduced with permission from Cortes and Jacob, Nat. Commun. **8**, 14144 (2017). Copyright 2017 Author(s), licensed under a Creative Commons Attribution-NonCommercial-NoDerivatives 4.0 International License. (d) Circuit-based HMM for realizing EIT between a dark atom and a bright atom. (e) Measured electric fields showing the long-range interaction between a bright atom and a dark atom. (f) The dependence of HMM-mediated EIT on the interatomic separation s. The red open (blue solid) circles are the measured (simulated) EIT split frequencies. Reproduced with permission from Guo *et al.*, Opt. Express 26, **627** (2018). Copyright 2018 OSA Publishing.

multilayered structures and metal nanowire arrays.[274,276] For example, a miniaturized biosensor has been fabricated using a gold/Al_2O_3 multilayered structure, as shown in Fig. 18(a). The thickness of the gold and Al_2O_3 layers were 16 nm and 30 nm, respectively.[276] The effective anisotropic permittivity tensor derived from EMT is shown in Fig. 18(b). For wavelengths in the range $520 \leq \lambda \leq 800$ nm, the signs of $\varepsilon_{\perp}$ and $\varepsilon_{//}$ are opposite, and therefore, the multilayered structure displays hyperbolic dispersion. The high-k modes in HMM are nonradiative and cannot be directly excited because of the momentum mismatch. Therefore, a grating or prism needs to be placed above the structure to provide additional transverse wave-vectors. For a TM wave incident on the structure, the reflectance spectra at different incidence angles are shown in Fig. 18(c). There are six prominent reflectance dips in the spectrum, which correspond to the six guided modes in the multilayered structure. Two guided modes below 500 nm are SPP modes while the other four guided modes are high-k modes in the HMM. The physical mechanism of this refractive index sensor is simple. When the refractive index of the surrounding medium changes, the coupling condition changes. This change can be directly determined by the shift of the resonance wavelength. The effective permittivity of the medium can be tuned by injecting different weight percentage concentrations of glycerol in distilled (DI) water. As a result, the reflectance spectrum of the HMM sensor shown in Fig. 18(d) was obtained. A red shift in resonance wavelength is observed when the glycerol weight percentage increases. Figures 18(e) and 18(f) give enlargements of Fig. 18(d) for the high-k modes in the HMM and the SPP modes, respectively. Comparing Fig. 18(e) with Fig. 18(f), it is evident that the high-k mode undergoes a significant shift in resonance wavelength, based on which the HMM sensor achieved a bulk refractive index sensitivity of 30 000 nm/RIU (per refractive index unit). The record figure of merit (FOM) can determine the sensitivity of the sensor,[276]

$$\mathrm{FOM} = (\Delta\lambda/\Delta n)(1/\Delta\omega), \tag{28}$$

where $\Delta\lambda$, $\Delta\omega$, and Δn denote the shift in wavelength, the width of the reflectance dip at half-maximum, and the change in refractive index, respectively. Larger values of FOM correspond to higher sensitivities. The FOM in Figs. 18(e) and 18(f) has values of 590 and 108, respectively, indicating that the high-k mode in the HMM is more sensitive to an extremely small refractive index change than the SPP.[276] In addition, the grating-coupled HMM biosensor can have higher angular sensitivity (with a maximum of 7000° per RIU) than traditional sensors, which is useful for angular detection of low molecular weight biomolecules.[277]

Recently, enhancement of the GH shift of a Gaussian beam reflected from a thin slab of Ag/TiO_2 HMM has been theoretically

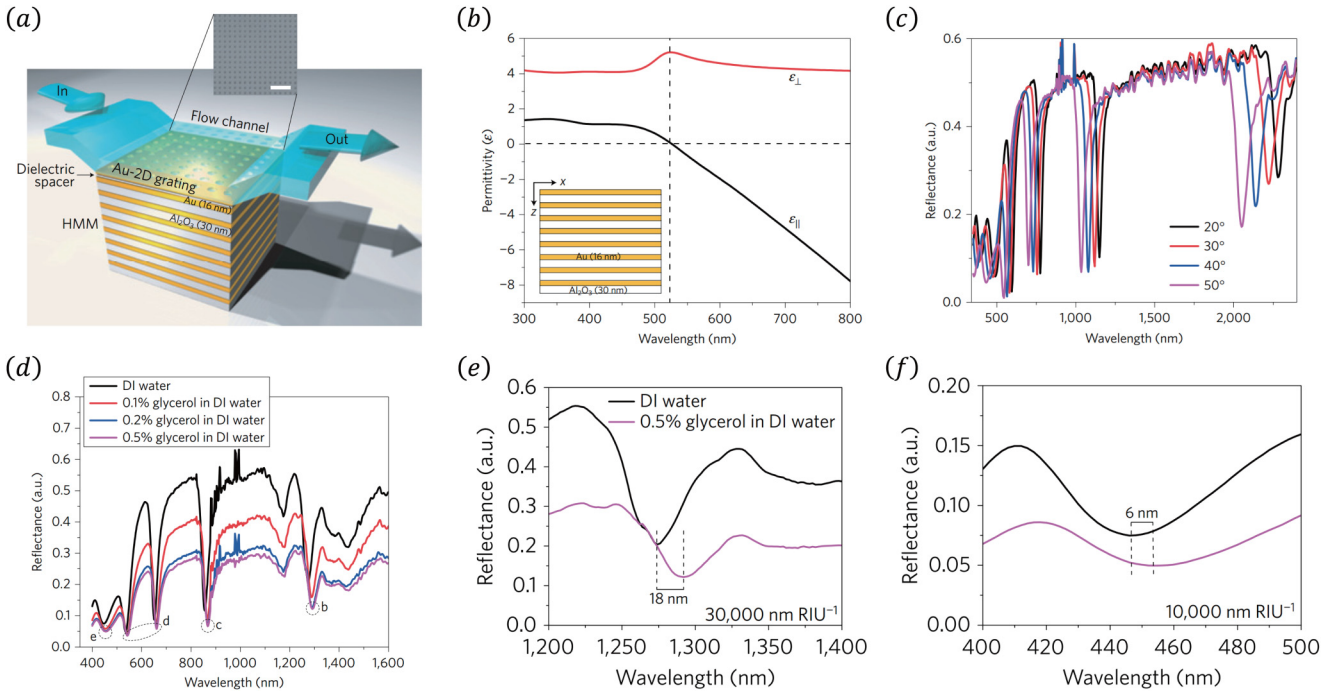

FIG. 18. (a) Schematic of a metal grating-coupled HMM sensor with a fluid flow channel. (b) Effective permittivity of the metal/dielectric multilayer structure. (c) Reflectance of the sensor at different incidence angles. (d) The reflectance of the sensor device obtained by injecting different weight percentage concentrations of glycerol in DI water. (e) Enlarged view of (d) from 1200 to 1400 nm. (f) As (e), but from 400–500 nm. Reproduced with permission from Sreekanth *et al.*, Nat. Mater. **15**, 621 (2016). Copyright 2016 Springer Nature.

proposed.[158] The GH shift of an HMM is calculated from[158,160]

$$s_{GH} = \frac{1}{k_{In}} \frac{d\Delta_\varphi}{d\theta}, \tag{29}$$

where $\Delta_\varphi = \varphi_e - \varphi_o$ denotes the phase difference between the ordinary wave and the extraordinary wave. k_{In} is the wave-vector in the incident medium and θ is the incidence angle. For the extraordinary wave, the reflection from the HMM disappears at the Brewster angle; the corresponding mode is called the Brewster mode.[158] Around the Brewster mode, there is an abrupt change in Δ_φ. As a result, $d\Delta_\varphi/d\theta$ becomes very large, which leads to an enhanced GH shift.[158,160] In another application of this effect, radiative refractive index sensors have been demonstrated in a microfluidic integrated HMM.[160]

VI. CONCLUSIONS

HMMs exhibit many fascinating properties, such as enhanced spontaneous radiation, all-angle negative refraction, and abnormal scattering phenomena. In recent years, they have been widely studied, with implementations based on subwavelength metal/dielectric multilayered structures, metal nanowire arrays, circuit systems, HMSs, and even natural hyperbolic media. The interesting properties of HMMs are directly associated with the special hyperbolic dispersion. By tuning topological transitions of the IFC, the interaction between light and matter can be significantly modified. In this tutorial, we have focused on three effective ways of manipulating the topological transition of IFCs: changing the frequency, tuning the imaginary part of the permittivity or permeability, and applying an external field. At the transition point from a closed elliptic IFC to an open hyperbolic IFC, a very flat elliptic IFC has been analyzed. Moreover, at the transition point from a metal-type hyperbolic IFC to a dielectric-type hyperbolic IFC, a linear-crossing IFC has been studied. The idea of dispersion manipulation in HMMs has been further extended to composite structures including HMMs. For example, a dispersionless bandgap can be realized in a 1D PHC based on the PVC condition. Dispersion manipulation in HMMs can be utilized in many applications, such as hyperlenses that can beat the diffraction limit, long-range energy transfer beyond the near-field coupling limit, and high-sensitivity sensors. Because of the unusual properties of HMMs, it is to be expected that still more novel optical devices based on HMMs will be developed in the future.

ACKNOWLEDGMENTS

This work was supported by the National Key R&D Program of China (Grant No. 2016YFA0301101), the National Natural Science Foundation of China (NSFC) (Grant Nos. 11774261, 11474220, and 61621001), the Natural Science Foundation of Shanghai (Grant No. 17ZR1443800), the Shanghai Science and Technology Committee (Grant No. 18JC1410900), and the China Postdoctoral Science Foundation (Grant Nos. 2019TQ0232 and 2019M661605).

REFERENCES

[1]A. Poddubny, I. Iorsh, P. Belov, and Y. Kivshar, Nat. Photonics **7**, 948 (2013).
[2]V. P. Drachev, V. A. Podolskiy, and A. V. Kildishev, Opt. Express **21**, 15048 (2013).
[3]P. Shekhar, J. Atkinson, and Z. Jacob, Nano Convergence **1**, 14 (2014).
[4]L. Ferrari, C. H. Wu, D. Lepage, X. Zhang, and Z. W. Liu, Prog. Quantum Electron. **40**, 1 (2015).
[5]D. R. Smith and D. Schurig, Phys. Rev. Lett. **90**, 077405 (2003).
[6]D. R. Smith, D. Schurig, J. J. Mock, P. Kolinko, and P. Rye, Appl. Phys. Lett. **84**, 2244 (2004).
[7]S. S. Kruk, Z. J. Wong, E. Pshenay-Severin, K. O'Brien, D. N. Neshev, Y. S. Kivshar, and X. Zhang, Nat. Commun. **7**, 11329 (2016).
[8]M. S. Mirmoosa, S. Y. Kosulnikov, and C. R. Simovski, Phys. Rev. B **94**, 075138 (2016).
[9]G. T. Papadaki, D. Fleischma, A. Davoyan, P. Yeh, and H. A. Atwater, Nat. Commun. **9**, 296 (2018).
[10]Y. H. Yang, P. F. Qin, B. Zheng, L. Shen, H. P. Wang, Z. J. Wang, E. P. Li, R. Singh, and H. S. Chen, Adv. Sci. **5**, 1801495 (2018).
[11]G. V. Naik, J. Liu, A. V. Kildishev, V. M. Shalaev, and A. Boltasseva, Proc. Natl. Acad. Sci. U.S.A. **109**, 8834 (2012).
[12]T. Xu, A. Agrawal, M. Abashin, K. J. Chau, and H. J. Lezec, Nature **497**, 470 (2013).
[13]C. Argyropoulos, N. M. Estakhri, F. Monticone, and A. Alù, Opt. Express **21**, 15037 (2013).
[14]A. A. High, R. C. Devlin, A. Dibos, M. Polking, D. S. Wild, J. Perczel, N. P. de Leon, M. D. Lukin, and H. Park, Nature **522**, 192 (2015).
[15]C. Sheng, H. Liu, H. Y. Chen, and S. N. Zhu, Nat. Commun. **9**, 4271 (2018).
[16]L. Sun, S. M. Feng, and X. D. Yang, Appl. Phys. Lett. **101**, 241101 (2012).
[17]S. M. Feng, Phys. Rev. Lett. **108**, 193904 (2012).
[18]S. H. Sedighy, C. Guclu, S. Campione, M. M. Amirhosseini, and F. Capolino, IEEE Trans. Microw. Theory Tech. **61**, 4110 (2013).
[19]H. Jiang, W. Liu, K. Yu, K. Fang, Y. Sun, Y. Li, and H. Chen, Phys. Rev. B **91**, 045302 (2015).
[20]Y. H. Yang, L. Q. Jing, L. Shen, Z. J. Wang, B. Zheng, H. P. Wang, E. P. Li, N. H. Shen, T. Koschny, C. M. Soukoulis, and H. S. Chen, NPG Asia Mater. **9**, e428 (2017).
[21]M. Memarian and G. V. Eleftheriades, Light Sci. Appl. **2**, e114 (2013).
[22]Z. W. Guo, H. T. Jiang, K. J. Zhu, Y. Sun, Y. H. Li, and H. Chen, Phys. Rev. Appl. **10**, 064048 (2018).
[23]Y. T. Yang, Z. Y. Jia, T. Xu, J. Luo, Y. Lai, and Z. H. Hang, Appl. Phys. Lett. **114**, 161905 (2019).
[24]Y. Cui, K. H. Fung, J. Xu, H. Ma, Y. Jin, S. L. He, and N. X. Fang, Nano Lett. **12**, 1443 (2012).
[25]J. Zhou, A. F. Kaplan, L. Chen, and L. J. Guo, ACS Photonics **1**, 618 (2014).
[26]X. Yin, G. Long, J. Li, H. Zhu, L. Chen, J. Guan, and X. Li, Sci. Rep. **5**, 15367 (2015).
[27]C. T. Riley, J. S. T. Smalley, J. R. J. Brodie, Y. Fainman, D. J. Sirbuly, and Z. W. Liu, Proc. Natl. Acad. Sci. U.S.A. **114**, 1264 (2017).
[28]N. Maccaferr, Y. Zhao, T. Isoniemi, A. Parracino, G. Strangi, and F. D. Angelis, Nano Lett. **19**, 1851 (2019).
[29]I. V. Iorsh, A. N. Poddubny, P. Ginzburg, P. A. Belov, and Y. S. Kivshar, Phys. Rev. Lett. **114**, 185501 (2015).
[30]H. Shen, D. Lu, B. VanSaders, J. J. Kan, H. X. Xu, E. E. Fullerton, and Z. W. Liu, Phys. Rev. X **5**, 021021 (2015).
[31]C. Qian, X. Lin, Y. Yang, F. Gao, Y. C. Shen, J. Lopez, I. Kaminer, B. L. Zhang, E. P. Li, M. Soljačić, and H. S. Chen, ACS Photonics **5**, 1506 (2018).
[32]Rituraj, P. B. Catrysse, and S. H. Fan, Opt. Express **27**, 3991 (2019).
[33]S. V. Zhukovsky, A. Andryieuski, J. E. Sipe, and A. V. Lavrinenko, Phys. Rev. B **90**, 155429 (2014).
[34]M. Mahmoodi S, H. Tavassoli, O. Takayama, J. Sukham, R. Malureanu, and A. V. Lavrinenko, Laser Photonics Rev. **13**, 1800253 (2019).
[35]O. Takayama and A. V. Lavrinenko, J. Opt. Soc. Am. B **36**, F38 (2019).
[36]M. A. Noginov, H. Li, Y. A. Barnakov, D. Dryden, G. Nataraj, G. Zhu, C. E. Bonner, M. Mayy, Z. Jacob, and E. E. Narimanov, Opt. Lett. **35**, 1863 (2010).
[37]T. Tumkur, G. Zhu, P. Black, Y. A. Barnakov, C. E. Bonner, and M. A. Noginov, Appl. Phys. Lett. **99**, 151115 (2011).

[38]H. N. Krishnamoorthy, Z. Jacob, E. Narimanov, I. Kretzschmar, and V. M. Menon, Science **336**, 205 (2012).
[39]T. Galfsky, H. N. S. Krishnamoorthy, W. Newman, E. E. Narimanov, Z. Jacob, and V. M. Menon, Optica **2**, 62 (2015).
[40]K. J. Feng, D. L. Sivco, and A. J. Hoffman, Opt. Express **26**, 4382 (2018).
[41]D. E. Fernandes, S. I. Maslovski, and M. G. Silveirinha, Phys. Rev. B **85**, 155107 (2012).
[42]F. Liu, L. Xiao, Y. Ye, M. X. Wang, K. Y. Cui, X. Feng, W. Zhang, and Y. D. Huang, Nat. Photonics **11**, 289 (2017).
[43]M. Silveirinha, Nat. Photonics **11**, 269 (2017).
[44]J. Tao, L. Wu, G. X. Zheng, and S. H. Yu, Carbon **150**, 136 (2019).
[45]Z. Jacob, L. V. Alekseyev, and E. Narimanov, Opt. Express **14**, 8247 (2006).
[46]Z. W. Liu, H. Lee, Y. Xiong, C. Sun, and X. Zhang, Science **315**, 1686 (2007).
[47]X. Zhang and Z. W. Liu, Nat. Mater. **7**, 435 (2008).
[48]D. L. Lu and Z. W. Liu, Nat. Commun. **3**, 1205 (2012).
[49]D. Lee, Y. D. Kim, M. Kim, S. So, H.-J. Choi, J. Mun, D. M. Nguyen, T. Badloe, J. G. Ok, K. Kim, H. Lee, and J. Rho, ACS Photonics **5**, 2549 (2018).
[50]V. Caligiuri, R. Dhama, K. V. Sreekanth, G. Strangi, and A. De Luca, Sci. Rep. **6**, 20002 (2016).
[51]V. Caligiuri and A. De Luca, J. Phys. D Appl. Phys. **49**, 08LT01 (2016).
[52]S.-A. Biehs, V. M. Menon, and G. S. Agarwal, Phys. Rev. B **93**, 245439 (2016).
[53]C. L. Cortes and Z. Jacob, Nat. Commun. **8**, 14144 (2017).
[54]R. Deshmukh, S.-A. Biehs, E. Khwaja, T. Galfsky, G. S. Agarwal, and V. M. Menon, ACS Photonics **5**, 2737 (2018).
[55]W. D. Newman, C. L. Cortes, A. Afshar, K. Cadien, A. Meldrum, R. Fedosejevs, and Z. Jacob, Sci. Adv. **4**, eaar5278 (2018).
[56]Z. W. Guo, H. T. Jiang, Y. H. Li, H. Chen, and G. S. Agarwal, Opt. Express **26**, 627 (2018).
[57]T. G. Folland, A. Fali, S. T. White, J. R. Matson, S. Liu, N. A. Aghamiri, J. H. Edgar, R. F. Haglund Jr, Y. Abate, and J. D. Caldwell, Nat. Commun. **9**, 4371 (2018).
[58]E. Yoxall, M. Schnell, A. Y. Nikitin, O. Txoperena, A. Woessner, M. B. Lundeberg, F. Casanova, L. E. Hueso, F. H. L. Koppens, and R. Hillenbrand, Nat. Photonics **9**, 674 (2015).
[59]J. D. Caldwell, I. Aharonovich, G. Cassabois, J. H. Edgar, B. Gil, and D. N. Basov, Nat. Rev. Mater. **4**, 552 (2019).
[60]A. Ambrosio, L. A. Jauregui, S. Dai, K. Chaudhary, M. Tamagnone, M. M. Fogler, D. N. Basov, F. Capasso, P. Kim, and W. L. Wilson, ACS Nano **11**, 8741 (2017).
[61]F. J. Alfaro-Mozaz, P. Alonso-González, S. Vélez, I. Dolado, M. Autore, S. Mastel, F. Casanova, L. E. Hueso, P. Li, A. Y. Nikitin, and R. Hillenbrand, Nat. Commun. **8**, 15624 (2017).
[62]X. Lin, Y. Yang, N. Rivera, J. J. López, Y. Shen, I. Kaminerb, H. Chen, B. Zhang, J. D. Joannopoulos, and M. Soljačić, Proc. Natl. Acad. Sci. U.S.A. **114**, 6717 (2017).
[63]W. Ma, P. Alonso-González, S. Li, A. Y. Nikitin, J. Yuan, J. Martín-Sánchez, J. Taboada-Gutiérrez, I. Amenabar, P. Li, S. Vélez, C. Tollan, Z. Dai, Y. Zhang, S. Sriram, K. Kalantar-Zadeh, S.-T. Lee, R. Hillenbrand, and Q. Bao, Nature **562**, 557 (2018).
[64]S. Y. Dai, M. Tymchenko, Y. F. Yang, Q. Ma, M. Pita-Vidal, K. Watanabe, T. Taniguchi, P. Jarillo-Herrero, M. M. Fogler, A. Alù, and D. N. Basov, Adv. Mater. **30**, 1706358 (2018).
[65]M. Tamagnone, A. Ambrosio, K. Chaudhary, L. A. Jauregui, P. Kim, W. L. Wilson, and F. Capasso, Sci. Adv. **4**, eaat7189 (2018).
[66]S. Y. Dai, J. M. Qin, G. W. Hu, C.-W. Qiu, T. H. Tao, X. Q. Li, and A. Alù, Nano Lett. **19**, 1009 (2019).
[67]E. E. Narimanov and A. V. Kildishev, Nat. Photonics **9**, 214 (2015).
[68]Z. Jacob, Nat. Mater. **13**, 1081 (2014).
[69]J. Sun, N. M. Litchinitser, and J. Zhou, ACS Photonics **1**, 293 (2014).
[70]L. Lu, R. E. Simpson, and S. K. Valiyaveedu, J. Opt. **20**, 103001 (2018).
[71]P. Huo, S. Zhang, Y. Liang, Y. Lu, and T. Xu, Adv. Opt. Mater. **7**, 1801616 (2019).
[72]J. S. T. Smalley, F. Vallini, X. Zhang, and Y. Fainman, Adv. Opt. Photonics **10**, 354 (2018).
[73]P. Cheben, R. Halir, J. H. Schmid, H. A. Atwater, and D. R. Smith, Nature **560**, 565 (2018).
[74]B. Wood, J. B. Pendry, and D. P. Tsai, Phys. Rev. B **74**, 115116 (2006).
[75]I. Avrutsky, I. Salakhutdinov, J. Elser, and V. Podolskiy, Phys. Rev. B **75**, 242402 (2007).
[76]A. A. Bogdanov and R. A. Suris, JETP Lett. **96**, 49 (2012).
[77]M. G. Silveirinha, Phys. Rev. E **73**, 046612 (2006).
[78]C. R. Simovski, P. A. Belov, A. V. Atrashchenko, and Y. S. Kivshar, Adv. Mater. **24**, 4229 (2012).
[79]M. E. Nasir, S. Peruch, N. Vasilantonakis, W. P. Wardley, W. Dickson, G. A. Wurtz, and A. V. Zayats, Appl. Phys. Lett. **107**, 121110 (2015).
[80]N. Vasilantonakis, M. E. Nasir, W. Dickson, G. A. Wurtz, and A. V. Zayats, Laser Photonics Rev. **9**, 345 (2015).
[81]P. Guo, R. P. Chang, and R. D. Schaller, Appl. Phys. Lett. **111**, 021108 (2017).
[82]S. S. Kruk, D. A. Powell, A. Minovich, D. N. Neshev, and Y. S. Kivshar, Opt. Express **20**, 15100 (2012).
[83]A. V. Chshelokova, P. V. Kapitanova, A. N. Poddubny, D. S. Filonov, A. P. Slobozhanyuk, Y. S. Kivshar, and P. A. Belov, J. Appl. Phys. **112**, 073116 (2012).
[84]A. V. Shchelokova, D. S. Filonov, P. V. Kapitanova, and P. A. Belov, Phys. Rev. B **90**, 115155 (2014).
[85]J. S. Gomez-Diaz, M. Tymchenko, and A. Alù, Opt. Express **5**, 2313 (2015).
[86]J. S. Gomez-Diaz, M. Tymchenko, and A. Alù, Phys. Rev. Lett. **114**, 233901 (2015).
[87]J. S. Gomez-Diaz and A. Alù, ACS Photonics **3**, 2211 (2016).
[88]A. Nemilentsau, T. Low, and G. Hanson, Phys. Rev. Lett. **116**, 066804 (2016).
[89]O. Y. Yermakov, A. I. Ovcharenko, M. Song, A. A. Bogdanov, I. V. Iorsh, and Y. S. Kivshar, Phys. Rev. B **91**, 235423 (2015).
[90]C. D. Hu, Z. Y. Li, R. Tong, X. X. Wu, Z. Xia, L. Wang, S. S. Li, Y. Z. Huang, S. X. Wang, B. Hou, C T Chan, and W. J. Wen, Phys. Rev. Lett. **121**, 024301 (2018).
[91]C. D. Hu, X. X. Wu, R. Tong, L. Wang, Y. Z. Huang, S. X. Wang, B. Hou, and W. J. Wen, NPG Asia Mater. **10**, 417 (2018).
[92]Y. H. Yang, P. F. Qin, X. Lin, E. P. Li, Z. J. Wang, B. L. Zhang, and H. S. Chen, Nat. Commun. **10**, 2002 (2019).
[93]P. X. Zheng, Q. Xu, X. Q. Su, D. Y. Wang, Y. H. Xu, X. Q. Zhang, Y. F. Li, Z. Tian, J. Q. Gu, L. Y. Liu, C. M. Ouyang, J. G. Han, and W. L. Zhang, Adv. Opt. Mater. **7**, 1801483 (2019).
[94]K. Feng, G. Harden, D. L. Sivco, and A. J. Hoffman, ACS Photonics **4**, 1621 (2017).
[95]K.-C. Shen, C.-T. Ku, C. Hsieh, H.-C. Kuo, Y.-J. Cheng, and D. P. Tsa, Adv. Mater. **30**, 1706918 (2018).
[96]R. Sohr, D. Wei, S. Tomasulo, M. K. Yakes, and S. Law, ACS Photonics **5**, 4003 (2018).
[97]E. E. Narimanov, Phys. Rev. X **4**, 041014 (2014).
[98]S. V. Zhukovsky, A. A. Orlov, V. E. Babicheva, A. V. Lavrinenko, and J. E. Sipe, Phys. Rev. A **90**, 013801 (2014).
[99]Y. R. He, S. L. He, J. Gao, and X. D. Yang, Opt. Express **20**, 22372 (2012).
[100]Y. R. He, S. L. He, and X. D. Yang, Opt. Lett. **37**, 2907 (2012).
[101]V. E. Babicheva, M. Y. Shalaginov, S. Ishii, A. Boltasseva, and A. V. Kildishev, Opt. Express **23**, 9681 (2015).
[102]V. E. Babicheva, M. Y. Shalaginov, S. Ishii, A. Boltasseva, and A. V. Kildishev, Opt. Express **23**, 31109 (2015).
[103]V. Caligiuri, L. Pezzi, A. Veltri, and A. De Luca, ACS Nano **11**, 1012 (2017).
[104]K. L. Tsakmakidis, A. D. Boardman, and O. Hess, Nature **450**, 397 (2007).
[105]H. Hu, D. Ji, X. Zeng, K. Liu, and Q. Gan, Sci. Rep. **3**, 1249 (2013).
[106]T. Xu and H. J. Lezec, Nat. Commun. **5**, 4141 (2014).
[107]X. Yin, H. Zhu, H. J. Guo, M. Deng, T. Xu, Z. J. Gong, X. Li, Z. H. Hang, C. Wu, H. Q. Li, S. Q. Chen, L. Zhou, and L. Chen, Laser Photonics Rev. **13**, 1800081 (2019).
[108]G. T. Papadakis and H. A. Atwater, Phys. Rev. B **92**, 184101 (2015).

[109]S. Dai, Q. Ma, M. K. Liu, T. Andersen, Z. Fei, M. D. Goldflam, M. Wagner, K. Watanabe, T. Taniguchi, M. Thiemens, F. Keilmann, G. C. A. M. Janssen, S.-E. Zhu, P. Jarillo-Herrero, M. M. Fogler, and D. N. Basov, Nat. Nanotechnol. **10**, 682 (2015).
[110]J. Brouillet, G. T. Papadakis, and H. A. Atwater, arxiv:1906.10663 (2019).
[111]C. Duncan, L. Perret, S. Palomba, M. Lapine, B. T. Kuhlmey, and C. Martijn de Sterke, Sci. Rep. **5**, 8983 (2015).
[112]A. N. Poddubny, I. V. Iorsh, and A. A. Sukhorukov, Phys. Rev. Lett. **117**, 123901 (2016).
[113]G. Marino, P. Segovia, A. V. Krasavin, P. Ginzburg, N. Olivier, G. A. Wurtz, and A. V. Zayats, Laser Photonics Rev. **12**, 1700189 (2018).
[114]V. R. Tuz, I. V. Fedorin, and V. I. Fesenko, Opt. Lett. **42**, 4561 (2017).
[115]A. Leviyev, B. Stein, A. Christofi, T. Galfsky, H. Krishnamoorthy, I. L. Kuskovsky, V. Menon, and A. B. Khanikaev, APL Photonics **2**, 076103 (2017).
[116]I. A. Kolmychek, A. R. Pomozov, A. P. Leontiev, K. S. Napolskii, and T. V. Murzina, Opt. Lett. **43**, 3917 (2018).
[117]V. I. Fesenko and V. R. Tuz, Phys. Rev. B **99**, 094404 (2019).
[118]W. L. Gao, M. Lawrence, B. Yang, F. Liu, F. Z. Fang, B. Béri, J. Li, and S. Zhang, Phys. Rev. Lett. **114**, 037402 (2015).
[119]M. Xiao, Q. Lin, and S. H. Fan, Phys. Rev. Lett. **117**, 057401 (2016).
[120]C. Shen, Y. Xie, N. Sui, W. Wang, S. A. Cummer, and Y. Jing, Phys. Rev. Lett. **115**, 254301 (2015).
[121]J. Christensen, F. J, and G. de Abajo, Phys. Rev. Lett. **108**, 124301 (2012).
[122]V. M. García-Chocano, J. Christensen, and J. Sánchez-Dehesa, Phys. Rev. Lett. **112**, 144301 (2014).
[123]J. Li, L. Fok, X. Yin, G. Bartal, and X. Zhang, Nat. Mater. **8**, 931 (2009).
[124]J. Qian, H.-X. Sun, S.-Q. Yuan, and X.-J. Liu, Appl. Phys. Lett. **114**, 013506 (2019).
[125]J. H. Oh, H. M. Seung, and Y. Y. Kima, Appl. Phys. Lett. **104**, 073503 (2014).
[126]H. W. Dong, S. D. Zhaoa, Y. S. Wanga, and C. Zhang, arXiv:1703.03298 (2017).
[127]R. Zhu, H. Yasuda, G. L. Huang, and J. K. Yang, Sci. Rep. **8**, 483 (2018).
[128]J. B. Pendry, Phys. Rev. Lett. **85**, 3966 (2000).
[129]D. R. Smith, J. B. Pendry, and M. C. K. Wiltshire, Science **305**, 788 (2004).
[130]J. B. Pendry, D. Schurig, and D. R. Smith, Science **312**, 1780 (2006).
[131]V. M. Shalaev, Nat. Photonics **1**, 41 (2007).
[132]I. Liberal and N. Engheta, Nat. Photonics **11**, 149 (2017).
[133]X. X. Niu, X. Y. Hu, S. S. Chu, and Q. H. Gong, Adv. Opt. Mater. **6**, 1701292 (2018).
[134]V. Caligiuri, R. Lento, L. Ricciardi, R. Termine, M. La Deda, S. Siprova, A. Golemme, and A. De Luca, Adv. Opt. Mater. **6**, 1701380 (2018).
[135]V. Caligiuri, M. Palei, M. Imran, L. Mann, and R. Krahne, ACS Photonics **5**, 2287 (2018).
[136]C. L. Cortes, W. Newman, S. Molesky, and Z. Jacob, J. Opt. **14**, 063001 (2012).
[137]G. S. Agarwal, *Quantum Statistical Theories of Spontaneous Emission and Their Relation to Other Approaches* (Springer, Berlin, 1974).
[138]I. Gontijo, M. Boroditsky, and E. Yablonovitch, Phys. Rev. B **60**, 11564 (1999).
[139]W. Vogel and D. G. Welsch, *Quantum Optics* (Wiley, Weinheim, 2006).
[140]E. M. Purcell, Phys. Rev. **69**, 37 (1946).
[141]A. N. Poddubny, P. A. Belov, and Y. S. Kivshar, Phys. Rev. A **84**, 023807 (2011).
[142]J. Kim, V. P. Drachev, Z. Jacob, G. V. Naik, A. Boltasseva, E. E. Narimanov, and V. M. Shalaev, Opt. Express **20**, 8100 (2012).
[143]A. N. Poddubny, P. A. Belov, P. Ginzburg, A. V. Zayats, and Y. S. Kivshar, Phys. Rev. B **86**, 035148 (2012).
[144]D. L. Lu, J. J. Kan, E. E. Fullerton, and Z. W. Liu, Nat. Nanotechnol. **9**, 48 (2014).
[145]L. Wang, S. L. Li, B. R. Zhang, Y. Z. Qin, Z. Tian, Y. F. Fang, Y. L. Li, Z. W. Liu, and Y. F. Mei, ACS Appl. Mater. Interfaces **10**, 7704 (2018).
[146]I. V. Lindell, *Methods for Electromagnetic Field Analysis* (Clarendon, Oxford, 1992).
[147]A. S. Potemkin, A. N. Poddubny, P. A. Belov, and Y. S. Kivshar, Phys. Rev. A **86**, 023848 (2012).
[148]K. Yu, Z. W. Guo, H. T. Jiang, and H. Chen, J. Appl. Phys. **119**, 203102 (2016).
[149]Z. W. Guo, H. T. Jiang, Y. Sun, Y. H. Li, and H. Chen, Appl. Sci. **8**, 596 (2018).
[150]E. C. Regan, Y. Igarashi, B. Zhen, I. Kaminer, C. W. Hsu, Y. Shen, J. D. Joannopoulos, and M. Soljačić, Sci. Adv. **2**, e1601591 (2016).
[151]D. Pidgayko, I. Sinev, D. Permyakovv, S. Sychev, F. Heyroth, V. Rutckaia, J. Schilling, A. Lavrinenko, A. Bogdanov, and A. Samusev, ACS Photonics **6**, 510 (2019).
[152]M. Silveirinha and N. Engheta, Phys. Rev. Lett. **97**, 157403 (2006).
[153]T. Zentgraf, Y. M. Liu, M. H. Mikkelsen, J. Valentine, and X. Zhang, Nat. Nanotechnol. **6**, 151 (2011).
[154]C. Sheng, H. Liu, Y. Wang, S. N. Zhu, and D. A. Genov, Nat. Photonics **7**, 902 (2013).
[155]M. Zhou, L. Shi, J. Zi, and Z. F. Yu, Phys. Rev. Lett. **115**, 023903 (2015).
[156]V. G. Veselago, Sov. Phys.-Uspekhi **10**, 509 (1968).
[157]J. Zhao, H. Zhang, X. Zhang, D. Li, H. Lu, and M. Xu, Photonics Res. **1**, 160 (2013).
[158]C. R. Xu, J. P. Xu, G. Song, C. J. Zhu, Y. P. Yang, and G. S. Agarwal, Opt. Express **24**, 21767 (2016).
[159]W. S. Zhang, W. J. Wu, S. Z. Chen, J. Zhang, X. H. Ling, W. X. Shu, H. L. Luo, and S. C. Wen, Photonics Res. **6**, 511 (2018).
[160]K. V. Sreekanth, P. Mahalakshmi, S. Han, M. S. M. Rajan, P. K. Choudhury, and R. Singh, Adv. Opt. Mater. **7**, 1900680 (2019).
[161]Z. C. Ruan and S. H. Fan, Phys. Rev. Lett. **105**, 013901 (2010).
[162]D. R. Smith, S. Schultz, P. Markoš, and C. M. Soukoulis, Phys. Rev. B **65**, 195104 (2002).
[163]A. A. Orlov, P. M. Voroshilov, P. A. Belov, and Y. S. Kivshar, Phys. Rev. B **84**, 045424 (2011).
[164]A. V. Chebykin, A. A. Orlov, A. V. Vozianova, S. I. Maslovski, Y. S. Kivshar, and P. A. Belov, Phys. Rev. B **84**, 115438 (2011).
[165]T. F. Li and J. B. Khurgin, Optica **3**, 1388 (2016).
[166]J. Elser and V. A. Podolskiya, Appl. Phys. Lett. **90**, 191109 (2007).
[167]R. J. Pollard, A. Murphy, W. R. Hendren, P. R. Evans, R. Atkinson, G. A. Wurtz, A. V. Zayats, and V. A. Podolskiy, Phys. Rev. Lett. **102**, 127405 (2009).
[168]R. Y. Liu, C. M. Roberts, Y. J. Zhong, V. A. Podolskiy, and D. Wasserman, ACS Photonics **3**, 1045 (2016).
[169]J. Schilling, Phys. Rev. E **74**, 046618 (2006).
[170]J. Elser, P. Wangberg, V. A. Podolskiy, and E. E. Narimanov, Appl. Rev. Lett. **89**, 261102 (2006).
[171]G. V. Eleftheriades, A. K. Iyer, and P. C. Kremer, IEEE Trans. Microw. **50**, 2702 (2002).
[172]C. Caloz and T. Itoh, *Electromagnetic Metamaterials Transmission Line Theory and Microwave Applications* (Wiley, New York, 2006).
[173]N. F. Yu and F. Capasso, Nat. Mater. **13**, 139 (2014).
[174]A. V. Kildishev, A. Boltasseva, and V. M. Shalaev, Science **339**, 1232009 (2013).
[175]Y. M. Liu and X. Zhang, Appl. Phys. Lett. **103**, 141101 (2013).
[176]O. Y. Yermakov, A. I. Ovcharenko, A. A. Bogdanov, I. V. Iorsh, K. Y. Bliokh, and Y. S. Kivshar, Phys. Rev. B **94**, 075446 (2016).
[177]J. S. T. Smalley, F. Vallini, S. A. Montoya, L. Ferrari, S. Shahin, C. T. Riley, B. Kanté, E. E. Fullerton, Z. Liu, and Y. Fainman, Nat. Commun. **8**, 13793 (2017).
[178]Y. Mazor and A. Alù, Phys. Rev. B **99**, 155425 (2019).
[179]Y. Mazor and A. Alù, Phys. Rev. B **99**, 045407 (2019).
[180]F. J. Rodríguez-Fortuño, G. Marino, P. Ginzburg, D. O'Connor, A. Martinez, G. A. Wurtz, and A. V. Zayats, Science **340**, 328 (2013).
[181]P. V. Kapitanova, P. Ginzburg, F. J. Rodríguez-Fortuño, D. S. Filonov, P. M. Voroshilov, P. A. Belov, A. N. Poddubny, Y. S. Kivshar, G. A. Wurtz, and A. V. Zayats, Nat. Commun. **5**, 3226 (2014).

[182]K. Y. Bliokh, D. Smirnova, and F. Nori, Science **348**, 1448 (2015).
[183]Z. W. Guo, H. T. Jiang, Y. Long, K. Yu, J. Ren, C. H. Xue, and H. Chen, Sci. Rep. **7**, 7742 (2017).
[184]Y. Long, J. Ren, and H. Chen, Proc. Natl. Acad. Sci. U.S.A. **115**, 9951 (2018).
[185]D. N. Basov, M. M. Fogler, and F. J. García de Abajo, Science **354**, aag1992 (2016).
[186]K. S. Novoselov, A. Mishchenko, A. Carvalho, and A. H. Castro Neto, Science **353**, aac9439 (2016).
[187]J. D. Caldwell, A. V. Kretinin, Y. G. Chen, V. Giannini, M. M. Fogler, Y. Francescato, C. T. Ellis, J. G. Tischler, and C. R. Woods, Nat. Commun. **5**, 5221 (2014).
[188]P. N. Li, M. Lewin, A. V. Kretinin, J. D. Caldwell, K. S. Novoselov, T. Taniguchi, K. Watanabe, F. Gaussmann, and T. Taubner, Nat. Commun. **6**, 7507 (2015).
[189]S. Dai, Q. Ma, T. Andersen, A. S. Mcleod, Z. Fei, M. K. Liu, M. Wagner, K. Watanabe, T. Taniguchi, M. Thiemens, F. Keilmann, P. Jarillo-Herrero, M. M. Fogler, and D. N. Basov, Nat. Commun. **6**, 6963 (2015).
[190]A. J. Giles, S. Dai, I. Vurgaftman, T. Hoffman, S. Liu, L. Lindsay, C. T. Ellis, N. Assefa, I. Chatzakis, T. L. Reinecke, J. G. Tischler, M. M. Fogler, J. H. Edgar, D. N. Basov, and J. D. Caldwell, Nat. Mater. **17**, 134 (2018).
[191]P. N. Li, I. Dolado, F. J. Alfaro-Mozaz, F. Casanova, L. E. Hueso, S. Liu, J. H. Edgar, A. Y. Nikitin, S. Vélez, and R. Hillenbrand, Science **359**, 892 (2018).
[192]A. J. Giles, S. Dai, O. J. Glembocki, A. V. Kretinin, Z. Sun, C. T. Ellis, J. G. Tischler, T. Taniguchi, K. Watanabe, M. M. Fogler, K. S. Novoselov, D. N. Basov, and J. D. Caldwell, Nano Lett. **16**, 3858 (2016).
[193]Z. Fei, A. S. Rodin, G. O. Andreev, W. Bao, A. S. McLeod, M. Wagner, L. M. Zhang, Z. Zhao, M. Thiemens, G. Dominguez, M. M. Fogler, A. H. Castro Neto, C. N. Lau, F. Keilmann, and D. N. Basov, Nature **487**, 82 (2012).
[194]P. Pons-Valencia, F. J. Alfaro-Mozaz, M. M. Wiecha, V. Biolek, I. Dolado, S. Vélez, P. Li, P. Alonso-González, F. Casanova, L. E. Hueso, L. Martín-Moreno, R. Hillenbrand, and A. Y. Nikitin, Nat. Commun. **10**, 3242 (2019).
[195]A. Woessner, M. B. Lundeberg, Y. Gao, A. Principi, P. Alonso-González, M. Carrega, K. Watanabe, T. Taniguchi, G. Vignale, M. Polini, J. Hone, R. Hillenbrand, and F. H. L. Koppens, Nat. Mater. **14**, 421 (2015).
[196]G. X. Ni, L. Wang, M. D. Goldflam, M. Wagner, Z. Fei, A. S. McLeod, M. K. Liu, F. Keilmann, B. Özyilmaz, A. H. Castro Neto, J. Hone, M. M. Fogler, and D. N. Basov, Nat. Photonics **10**, 244 (2016).
[197]V. B. Brar, M. S. Jang, M. Sherrott, S. Kim, J. J. Loepz, L. B. Kim, M. Choi, and H. Atwater, Nano Lett. **14**, 3876 (2014).
[198]Z. B. Zheng, J. N. Chen, Y. Wang, X. M. Wang, X. B. Chen, P. Y. Liu, J. B. Xu, W. G. Xie, H. J. Chen, S. Z. Deng, and N. S. Xu, Adv. Mater. **30**, 1705318 (2018).
[199]Z. B. Zheng, N. S. Xu, S. L. Oscurato, M. Tamagnone, F. S. Sun, Y. Z. Jiang, Y. L. Ke, J. N. Chen, W. C. Huang, W. L. Wilson, A. Ambrosio, S. Z. Deng, and H. J. Chen, Sci. Adv. **5**, eaav8690 (2019).
[200]S. Dai, Z. Fei, Q. Ma, A. S. Rodin, M. Wagner, A. S. Mcleod, M. K. Liu, W. Gannett, W. Regan, K. Watanabe, T. Taniguchi, M. Thiemens, G. Dominguez, A. H. C. Neto, A. Zettl, F. Keilmann, P. Jarillo-Herrero, M. M. Fogler, and D. N. Basov, Science **343**, 1125 (2014).
[201]B. Peng, ŞK Özdemir, S. Rotter, H. Yilmaz, M. Liertzer, F. Monifi, C. M. Bender, F. Nori, and L. Yang, Science **346**, 328 (2014).
[202]A. Guo, G. J. Salamo, D. Duchesne, R. Morandotti, M. Volatier-Ravat, V. Aimez, G. A. Siviloglou, and D. N. Christodoulides, Phys. Rev. Lett. **103**, 093902 (2009).
[203]N. H. Shen, P. Zhang, T. Koschny, and C. M. Soukoulis, Phys. Rev. B **93**, 245118 (2016).
[204]M. A. Vincenti, D. de Ceglia, V. Rondinone, A. Ladisa, A. D'Orazio, M. J. Bloemer, and M. Scalora, Phys. Rev. A **80**, 053807 (2009).
[205]X. J. Ni, S. Ishii, M. D. Thoreson, V. M. Shalaev, S. Han, S. Lee, and A. V. Kildishev, Opt. Express **19**, 25242 (2011).
[206]A. Vakil and N. Engheta, Science **332**, 1291 (2011).
[207]F. J and G. de Abajo, ACS Photonics **1**, 135 (2014).
[208]Y. C. Fan, N. H. Shen, F. L. Zhang, Q. Zhao, H. J. Wu, Q. H. Fu, Z. Y. Wei, H. Q. Li, and C. M. Soukoulis, Adv. Opt. Mater. **7**, 1800537 (2019).
[209]Y. C. Fan, N. H. Shen, T. Koschny, and C. M. Soukoulis, ACS Photonics **2**, 151 (2015).
[210]Y. C. Fan, N. H. Shen, F. L. Zhang, Q. Zhao, Z. Y. Wei, J. J. Dong, Q. H. Fu, H. Q. Li, and C. M. Soukoulis, ACS Photonics **5**, 1612 (2018).
[211]Y. Long, Z. R. Zhang, and X. P. Su, Europhys. Lett. **116**, 37004 (2016).
[212]K. V. Sreekanth, A. De Luca, and G. Strangi, Appl. Phys. Lett. **103**, 023107 (2013).
[213]A. Tyszka-Zawadzka, B. Janaszek, and P. Szczepański, Opt. Express **25**, 7263 (2017).
[214]M. Shoaei, M. K. Moravvej-Farshi, and L. Yousefi, J. Opt. Soc. Am. B **32**, 2358 (2015).
[215]Y.-C. Chang, C.-H. Liu, C.-H. Liu, S. Y. Zhang, S. R. Marder, E. E. Narimanov, Z. H. Zhong, and T. B. Norris, Nat. Commun. **7**, 10568 (2016).
[216]B. Janaszek, A. Tyszka-Zawadzka, and P. Szczepański, Opt. Express **24**, 24129 (2016).
[217]J. Ran, Y. W. Zhang, X. D. Chen, K. Fang, J. F. Zhao, Y. Sun, and H. Chen, Sci. Rep. **5**, 11659 (2015).
[218]J. Ran, Y. W. Zhang, X. D. Chen, K. Fang, J. F. Zhao, and H. Chen, Sci. Rep. **6**, 23973 (2016).
[219]J. Ran, Y. W. Zhang, X. D. Chen, and H. Chen, IEEE Microw. Wirel. Compon. Lett. **28**, 43 (2018).
[220]Q. Cheng, W. X. Jiang, and T. J. Cui, Phys. Rev. Lett. **108**, 213903 (2012).
[221]H. F. Ma, J. H. Shi, W. X. Jiang, and T. J. Cui, Appl. Phys. Lett. **101**, 253513 (2012).
[222]J. Luo, P. Xu, H. Y. Chen, B. Hou, L. Gao, and Y. Lai, Appl. Phys. Lett. **100**, 221903 (2012).
[223]J. Luo and Y. Lai, Sci. Rep. **4**, 5875 (2015).
[224]G. Lipworth, J. Ensworth, K. Seetharam, J. S. Lee, P. Schmalenberg, T. Nomura, M. S. Reynolds, D. R. Smith, and Y. Urzhumov, Sci. Rep. **5**, 12764 (2015).
[225]K. Zhang, J. H. Fu, L.-Y. Xiao, Q. Wu, and L.-W. Li, J. Appl. Phys. **113**, 084908 (2013).
[226]S. M. Zhong, Y. G. Ma, and S. L. He, Appl. Phys. Lett. **105**, 023504 (2014).
[227]J. Luo, W. X. Lu, Z. H. Hang, H. Y. Chen, B. Hou, Y. Lai, and C. T. Chan, Phys. Rev. Lett. **112**, 073903 (2014).
[228]A. S. Shalin, P. Ginzburg, A. A. Orlov, I. Iorsh, P. A. Belov, Y. S. Kivshar, and A. V. Zayats, Phys. Rev. B **91**, 125426 (2015).
[229]X. J. Zhang and Y. Wu, Sci. Rep. **5**, 7892 (2015).
[230]Y. Li, H. T. Jiang, W. W. Liu, J. Ran, Y. Lai, and H. Chen, Europhys. Lett. **113**, 57006 (2016).
[231]F. S. Deng, Y. M. Li, Y. Sun, X. Wang, Z. W. Guo, Y. L. Shi, H. T. Jiang, K. Chang, and H. Chen, Opt. Lett. **40**, 3380 (2015).
[232]Q. H. Guo, W. L. Gao, J. Chen, Y. M. Liu, and S. Zhang, Phys. Rev. Lett. **115**, 067402 (2015).
[233]Y. M. Zhang, Y. Luo, J. B. Pendry, and B. L. Zhang, Phys. Rev. Lett. **123**, 067701 (2019).
[234]E. Yablonovitch, Phys. Rev. Lett. **58**, 2059 (1987).
[235]S. John, Phys. Rev. Lett. **58**, 2486 (1987).
[236]Y. Fink, J. N. Winn, S. Fan, C. Chen, J. Michel, J. D. Joannopoulos, and E. L. Thomas, Science **282**, 1679 (1998).
[237]J. Li, L. Zhou, C. T. Chan, and P. Sheng, Phys. Rev. Lett. **90**, 083901 (2003).
[238]H. T. Jiang, H. Chen, H. Q. Li, and Y. W. Zhang, Appl. Rev. Lett. **83**, 5386 (2003).
[239]S. Kocaman, R. Chatterjee, N. C. Panoiu, J. F. McMillan, M. B. Yu, R. M. Osgood, D. L. Kwong, and C. W. Wong, Phys. Rev. Lett. **102**, 203905 (2009).
[240]S. Kocaman, M. S. Aras, P. Hsieh, J. F. McMillan, C. G. Biris, N. C. Panoiu, M. B. Yu, D. L. Kwong, A. Stein, and C. W. Wong, Nat. Photonics **5**, 499 (2011).
[241]H.-T. Jiang, Y.-H. Li, Z.-G. Wang, Y.-W. Zhang, and H. Chen, Philos. Mag. **92**, 1317 (2012).
[242]H. T. Jiang, H. Chen, H. Q. Li, Y. W. Zhang, J. Zi, and S. Y. Zhu, Phys. Rev. E **69**, 066607 (2004).

[243]L.-G. Wang, H. Chen, and S.-Y. Zhu, Phys. Rev. B **70**, 245102 (2004).
[244]Y. J. Xiang, X. Y. Dai, and S. C. Wen, J. Opt. Soc. Am. B **24**, 2033 (2007).
[245]Y. J. Xiang, X. Y. Dai, S. C. wen, and D. Y. Fan, J. Appl. Phys. **102**, 093107 (2007).
[246]C. Xue, Y. Ding, H. Jiang, Y. Li, Z. Wang, Y. Zhang, and H. Chen, Phys. Rev. B **93**, 125310 (2016).
[247]F. Wu, G. Lu, C. H. Xue, H. T. Jiang, Z. W. Guo, M. J. Zheng, C. X. Chen, G. Q. Du, and H. Chen, Appl. Phys. Lett. **112**, 041902 (2018).
[248]F. Wu, G. Lu, Z. W. Guo, H. T. Jiang, C. H. Xue, M. J. Zheng, C. X. Chen, G. Q. Du, and H. Chen, Phys. Rev. Appl. **10**, 064022 (2018).
[249]C. H. Xue, F. Wu, H. T. Jiang, Y. H. Li, Y. W. Zhang, and H. Chen, Sci. Rep. **6**, 39418 (2016).
[250]M. E. Sasin, R. P. Seisyan, M. A. Kalitteevski, S. Brand, R. A. Abram, J. M. Chamberlain, A. Y. Egorov, A. P. Vasil'ev, V. S. Mikhrin, and A. V. Kavokin, Appl. Phys. Lett. **92**, 251112 (2008).
[251]T. H. Feng, Y. H. Li, H. T. Jiang, Y. Sun, L. He, H. Q. Li, Y. W. Zhang, Y. L. Shi, and H. Chen, Phys. Rev. E **79**, 026601 (2009).
[252]Q. Huang, Z. Guo, J. Feng, C. Yu, H. Jiang, Z. Zhang, Z. Wang, and H. Chen, Laser Photonics Rev. **1**, 1800339 (2019).
[253]G. Lu, F. Wu, M. J. Zheng, C. X. Chen, X. C. Zhou, C. Diao, F. Liu, G. Q. Du, C. H. Xue, H. T. Jiang, and H. Chen, Opt. Express **27**, 5326 (2019).
[254]E. E. Narimanov, Faraday Discuss. **178**, 45 (2015).
[255]J. J. Wu, F. Wu, C. H. Xue, Z. W. Guo, H. T. Jiang, Y. Sun, Y. H. Li, and H. Chen, Opt. Express **27**, 24835 (2019).
[256]Z. Huang and E. E. Narimanov, Appl. Rev. Lett. **105**, 031101 (2014).
[257]V. N. Smolyaninova, B. Yost, D. Lahneman, E. E. Narimanov, and I. I. Smolyaninov, Sci. Rep. **4**, 5706 (2015).
[258]T. Galfsky, Z. Sun, C. R. Considine, C.-T. Chou, W.-C. Ko, Y.-H. Lee, E. E. Narimanov, and V. M. Menon, Nano Lett. **16**, 4940 (2016).
[259]T. Galfsky, J. Gu, E. E. Narimanov, and V. M. Menon, Proc. Natl. Acad. Sci. U.S.A. **114**, 5125 (2017).
[260]J.-R. Wang, X.-D. Chen, F.-L. Zhao, and J.-W. Dong, Sci. Rep. **6**, 22739 (2016).
[261]X.-D. Chen, W.-M. Deng, F.-L. Zhao, and J.-W. Dong, Laser Photonics Rev. **12**, 1800073 (2018).
[262]N. Fang, H. Lee, C. Sun, and X. Zhang, Science **308**, 534 (2005).
[263]I. I. Smolyaninov, Y. J. Hung, and C. C. Davis, Science **315**, 1699 (2007).
[264]Y. Xiong, Z. W. Liu, and X. Zhang, Appl. Phys. Lett. **94**, 203108 (2009).
[265]J. B. Sun and N. M. Litchinitster, ACS Nano **12**, 542 (2018).
[266]B. D. F. Casse, W. T. Lu, Y. J. Huang, E. Gultepe, L. Menon, and S. Sridhar, Appl. Phys. Lett. **96**, 023114 (2010).
[267]J. G. Hayashi, A. Stefani, S. Antipov, R. Lwin, S. D. Jackson, D. D. Hudson, S. Fleming, A. Argyros, and B. T. Kuhlmkey, Opt. Express **27**, 21420 (2019).
[268]Q. He, S. Y. Xiao, and L. Zhou, Opt. Express **21**, 28948 (2013).
[269]P. W. Milonni, *The Quantum Vacuum* (Academic Press, New York, 1994).
[270]A. I. Volokitin and B. N. J. Persson, Rev. Mod. Phys. **79**, 1291 (2007).
[271]S. Zhang, D. A. Genov, Y. Wang, M. Liu, and X. Zhang, Phys. Rev. Lett. **101**, 047401 (2008).
[272]N. Liu, L. Langguth, T. Weiss, J. Kästel, M. Fleischhauer, T. Pfau, and H. Giessen, Nat. Mater. **8**, 758 (2009).
[273]N. Liu, T. Weiss, M. Mesch, L. Langguth, U. Eigenthaler, M. Hirscher, C. Sönnichsen, and H. Giessen, Nano Lett. **10**, 1103 (2010).
[274]A. V. Kabashin, P. Evans, S. Pastkovsky, W. Hendren, G. A. Wurtz, R. Atkinson, R. Pollard, V. A. Podolskiy, and A. V. Zayats, Nat. Mater. **8**, 867 (2009).
[275]N. Vasilantonakis, G. A. Wurtz, V. A. Podolskiy, and A. V. Zayats, Opt. Express **23**, 14329 (2015).
[276]K. V. Sreekanth, Y. Alapan, M. ElKabbash, E. Ilker, M. Hinczewski, U. A. Gurkan, A. De Luca, and G. Strangi, Nat. Mater. **15**, 621 (2016).
[277]K. V. Sreekanth, Y. Alapan, M. ElKabbash, A. M. Wen, E. Ilker, M. Hinczewski, U. A. Gurkan, N. F. Steinmetz, and G. Strangi, Adv. Opt. Mater. **4**, 1767 (2016).
[278]K. V. Sreekanth, M. ElKabbash, Y. Alapan, E. I. Ilker, M. Hinczewski, U. A. Gurkan, and G. Strangi, EPJ Appl. Metamaterials **4**, 1 (2017).
[279]K. V. Sreekanth, Q. L. Ouyang, S. Sreejith, S. W. Zeng, W. Lishu, E. Ilker, W. L. Dong, M. ElKabbash, Y. Ting, C. T. Lim, M. Hinczewski, G. Strangi, K.-T. Yong, R. E. Simpson, and R. Singh, Adv. Opt. Mater. **7**, 1900081 (2019).
[280]X. J. Jiang, T. Wang, L. Cheng, Q. F. Zhong, R. Q. Yan, and X. Huang, Opt. Express **27**, 18970 (2019).